

Flat Bands from Diffraction in Periodic Systems

Joel Lehtikainen ¹, Rebecca Heilmann ¹, Aron J. J. Dahlberg ¹, Eero Härmä ¹, Malek Mahmoudi ², Arpan Dutta ^{2,*}, Konstantinos S. Daskalakis ² and Päivi Törmä ^{1,†}

¹*Department of Applied Physics, Aalto University School of Science, P.O. Box 15100, Aalto, FI-00076, Finland*

²*Department of Mechanical and Materials Engineering, University of Turku, FI-20014 Turku, Finland*

(Dated: February 26, 2026)

Periodic photonic structures enable precise control over the light–matter interaction through band structure engineering. Certain lattice geometries exhibit dispersionless flat bands, characterized by vanishing group velocity and diverging density of states, which present unique opportunities for applications such as slow light, nonlinear optical processes and controlling photoluminescence. However, thus far, flat bands have not been reported in systems where the lattice sites are radiatively coupled over a long range. Here we show that lattices consisting of superposed equispaced one dimensional chains exhibit flat bands with a purely diffractive origin, with the energies and angles of the flat bands controlled by the geometrical parameters of the lattice and the unit cell. The flat bands extend over all angles, can have linewidths on the order of a few nanometers, and are linearly polarized. We experimentally observe flat bands at predicted energies in lattices of gold nanoparticles at near-infrared frequencies using Fourier spectroscopy. Our results provide a general and efficient design strategy for lattices with flat, polarized dispersions for applications such as flat-band lasing, enhancing light–matter interaction, and controlling the emission or absorption of electromagnetic radiation over a wide spectral range.

I. INTRODUCTION

Waves propagating in spatially periodic structures exhibit discrete band structures, with each band having its own dispersion relation $E_m(\mathbf{k})$, linking the energy of the m th band E_m to the wavevector \mathbf{k} . *Flat bands* are dispersionless bands for which $E_m(\mathbf{k}) = E_0$ at least over some range of the wavevector \mathbf{k} (or angle of propagation). On a flat band, the group velocity vanishes and the density of states diverges. These properties pave the way for several interesting applications: stronger nonlinear optical processes [1, 2], optical signal processing components [3], diffraction-free transport of images [4], and increasing the rate of spontaneous emission [5, 6] and absorption [7]. For overviews of recent research in the field, see reviews [8–10]. Although many systems in fact have only quasi-flat bands ($E_m(\mathbf{k}) \approx E_0$), for the sake of brevity, hereinafter we use the term “flat bands”. The first theoretical predictions of tight-binding (coupling between lattice sites limited to the nearest or a few neighbors) systems date from the 1980s, first in a quasiperiodic tiling [11], then in any frustrated two dimensional (2D) lattices [12], a category that includes the extensively studied Lieb lattice [13]. Lieb showed for the Lieb lattice, and Mielke for line graph lattices such as the kagome lattice [14], that these lattices have a ferromagnetic flat-band ground state. Further algorithms have been developed to construct lattices within the tight-binding assumption with flat-band states [15–18]. Interest in flat bands grew rapidly after observation of strongly correlated and superconducting states in flat bands of graphene moiré systems [19–24].

Advances in nanofabrication techniques permitted experimental realizations of photonic flat bands starting from 2014 in lattices of parallel waveguides [4, 25–29], coupled metallic resonators [30–32], short-lived exciton–polaritons [33–35], photonic moiré lattices [2, 36–41], strained photonic crystals [42], photonic crystals with disorder [43], photonic crystals exploiting rotational degrees of freedom [44] or by using metasurface-on-a-waveguide structures [6, 7, 45–52]. Of these systems, lattices of waveguides, photonic moiré lattices, coupled metallic resonators, and exciton–polariton systems can be considered as emulators of tight-binding systems, because they restrict the effective coupling range between lattice sites through evanescent coupling (lattices of waveguides and photonic moiré lattices), physical couplings (coupled metallic resonators), or short lifetime of exciton–polaritons. In the metasurface–waveguide structures, the guided modes of the waveguide are coupled to the free space modes by the metasurface. The bands are flattened by (i) the refractive index contrast with the surrounding medium [45, 49], (ii) by coupling of the odd and even guided modes of the waveguide through breaking of vertical symmetry [6, 7, 46–48, 51], or (iii) by using strong coupling [50]. In strained photonic crystals, a strain-induced pseudoelectromagnetic field flattens the dispersions of the Landau levels [42]. In photonic crystals exploiting disorder, the flat band forms from band folding caused by the superperiodicity and the emergence of multiple quasi-bound states in the continuum (qBICs).

Here, we introduce general principles to generate lattice geometries with flat bands at desired energies and angles in systems where lattice sites are radiatively coupled over a long range. The flat bands originate solely from diffraction by the lattice, and are therefore different from those described in the previous paragraph. A geometry is depicted in [Fig. 1(a)] and experimental demonstration

* Present address: Nanoscience Center and Department of Physics, University of Jyväskylä, P.O. Box 35, 40014, Jyväskylä, Finland

† Contact author: paivi.torma@aalto.fi

of the concept is shown in [Fig. 1(b)]; for comparison, examples other types of flat-band generating systems are given in [Figs. 1(c)–(d)]. The flat bands generated by our approach are approximately flat ($E(\mathbf{k}) \approx \text{const.}$) at all or desired values of the wavevector \mathbf{k} ; the flatness and angular extent are controlled by the lattice geometry, given by the general design principles expressed in analytical formulas. As the platform for experimental verification, we chose plasmonic nanoparticle lattices. Their collective optical modes, called surface lattice resonances (SLRs), are hybrids of single-nanoparticle plasmonic resonances and diffraction orders of the periodic structure [53–56]. The SLR modes follow quite closely the diffraction condition, and they can be approximately described by the *empty lattice approximation* where the effects of a non-trivial unit cell are taken into account by a structure factor that modifies the simple diffraction condition [57]. We use the empty lattice approximation to calculate the band structures and to guide the design of the lattice geometries.

This paper is organized as follows: in Section II, we use the rectangular lattice as an illustrative example of how flat bands are formed within the empty lattice approximation and formulate predictions of the properties of the flat bands. In Section III A, we present *chain lattices*, a category of lattice geometries that exhibit flat bands at angles and energies controlled by the lattice geometry. Sections III B–III H explore examples of chain lattices to study how the lattice parameters affect the band structure. We experimentally demonstrate the feasibility of the proposed concepts with plasmonic nanoparticle arrays for selected examples. As a summary, rules for designing lattices with flat bands are presented in Section III I. Finally, conclusions and an outlook are given in Section IV.

II. FLAT BANDS IN THE EMPTY LATTICE APPROXIMATION

We calculate the band structures of the investigated lattice geometries using the empty lattice approximation [57], which consists of superposing the dispersion of the diffracted waves in a homogeneous optical background weighted with the structure factor of each mode. This approach assumes that each lattice site causes scattering of the light, and is thus general for any type of approximately pointlike scatterers. We denote the number and position of unit cells of the lattice by N_L and \mathbf{R}_n , respectively, and the number of sites in the unit cell and their distances from \mathbf{R}_n by N_u and δ_j , respectively. The structure factor $S_{\text{tot}}(\mathbf{k})$ describes the intensity of

scattering by the lattice to the mode \mathbf{k} and is defined as

$$\begin{aligned} S_{\text{tot}}(\mathbf{k}) &= \frac{1}{(N_L N_u)^2} \left| \sum_{n=1}^{N_L} \sum_{j=1}^{N_u} e^{i\mathbf{k} \cdot (\mathbf{R}_n + \delta_j)} \right|^2 \\ &= \frac{1}{N_u^2} \left| \sum_{j=1}^{N_u} e^{i\mathbf{k} \cdot \delta_j} \right|^2 \frac{1}{N_L^2} \left| \sum_{n=1}^{N_L} e^{i\mathbf{k} \cdot \mathbf{R}_n} \right|^2 \\ &= \frac{1}{N_u^2} \left| \sum_{j=1}^{N_u} e^{i\mathbf{k} \cdot \delta_j} \right|^2 \sum_{\mathbf{G}} \delta(\mathbf{k} - \mathbf{G}) \\ &\equiv S(\mathbf{k}) \sum_{\mathbf{G}} \delta(\mathbf{k} - \mathbf{G}), \end{aligned} \quad (1)$$

where \mathbf{G} indicates the reciprocal lattice vectors and δ is the Kronecker delta. The second-to-last equality holds for periodic and infinite lattices, for which the structure factor $S(\mathbf{k})$ can take nonzero values only at the sites of the reciprocal lattice [58]. However, it is approximately valid also in sufficiently large finite lattices, as can be seen from the excellent match between theory and experiment in the following sections. In essence, Eq. (1) tells that the geometric arrangement of the scatterers within the unit cell can be used for controlling the value of the structure factor, that is, the weight of the mode. The structure factor can take values between 0 and 1. In the following, we consider always the part of the structure factor related to the unit cell $S(\mathbf{k})$.

In addition to the strength of the scattering to a particular mode, we are also interested in the polarization state of the diffracted light. If the scatterers can be taken to radiate as electric dipoles—as is the case, for example, with sub-wavelength-sized plasmonic nanoparticles—diffraction in (out) of the plane of incidence corresponds to linearly TE (TM) polarized light. See Fig. 1(c) for an example: light incident on the lattice in the yz plane and s polarized (p polarized) will induce in-plane dipolar excitations in the x (y) direction in the nanoparticles, leading to x - (y -)polarized diffracted light. As the in-plane momentum is determined by the plane of incidence to be along y , the diffracted light is TE (TM) polarized with respect to this direction [56, 59, 60]. The SLRs arising from diffraction orders in (out of) the plane of incidence are customarily correspondingly called TE (TM) modes. Unpolarized light excites both TE and TM modes.

To assign a quantitative approximant for the polarization state of the mode with the in-plane wavevector (k_x, k_y) and assuming the plane of incidence to be the yz plane, we define the TE polarization fraction p_{TE} as

$$p_{\text{TE}} \equiv \begin{cases} 1, & \text{if } k_x = k_y = 0, \\ \frac{|k_y|}{|k_y| + |k_x|}, & \text{otherwise.} \end{cases} \quad (2)$$

If the xz plane is taken to be the plane of incidence, the x and y components are swapped.

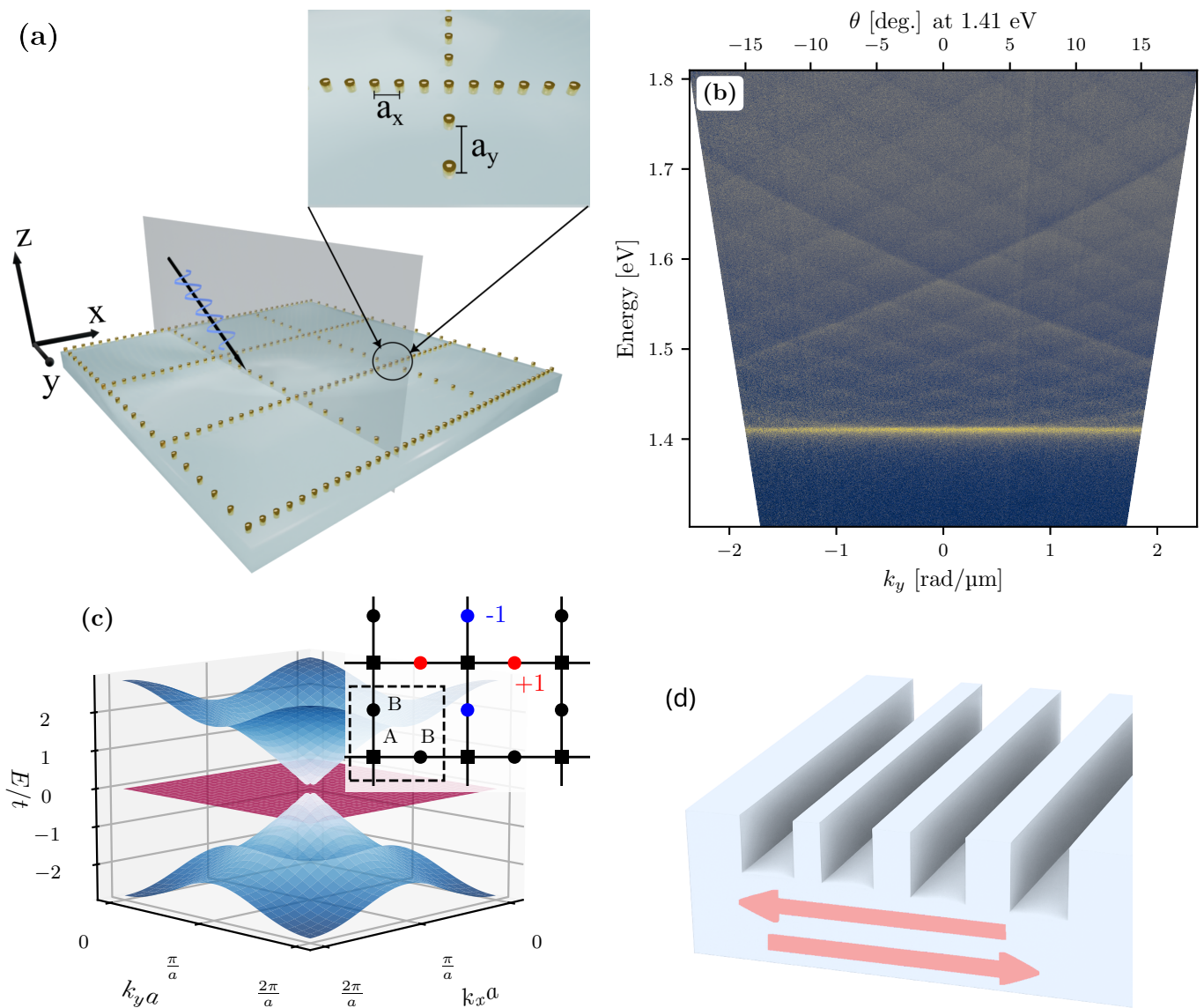


FIG. 1. Schematic figure of the various means of achieving photonic flat bands. Panel (a) depicts an example of the class of flat-band lattices we propose: a rectangular chain lattice, realized here by gold nanocylinders, that diffracts incident white light preferentially into a narrow-linewidth flat band of a specified polarization. The gray plane is the plane of incidence (yz plane) and here the incident light is s -polarized (in the x direction). Panel (b) presents an experimentally observed flat band in such a geometry, discussed further in Section III B. The in-plane momentum k_y corresponds to the angle of light emission/absorption by the lattice. The color scale from blue (minimum) to yellow (maximum) shows the extinction of the array in TM polarization. Panel (c) shows a tight-binding emulating system; its top right part depicts the lattice structure of the Lieb lattice, indicating its bipartite division into A (squares) and B sites (circles). The dashed rectangle shows the unit cell of the lattice. The red and blue colors indicate the amplitudes of the wavefunction at the B sites surrounding a single A site. Hopping to the A site is inhibited by destructive interference. The bottom part shows the dispersions of the three energy bands, including one exactly flat band, of the Hubbard model of the Lieb lattice. Panel (d) depicts counterpropagating guided modes (red arrows) in a metasurface-waveguide structure. The metasurface couples the odd and even modes of the waveguide, and the interference of the counterpropagating modes flattens the dispersion [6]. In some metasurface-waveguide systems, the flattening emerges via the index contrast between the guided mode and the surrounding medium [45, 49] (not depicted here).

Selecting the lattice positions $\{\mathbf{r}_n\}$ to produce a given structure factor profile $S(\mathbf{k})$ (and band structure) is an ill-posed problem and cannot be solved by analytical inversion. To tackle this problem, we make ansätze to find lattices with flat bands and progressively make the lat-

tice geometry more complex based on intuition obtained from the analytical form of the structure factor. To this end, we present an example below.

To illustrate how the superposition of diffracting modes can form flat bands, we consider the rectangular

lattice: Figure 2(a) shows the dispersion of a rectangular lattice, with lattice constants $a_y = 5a_x$, along the line $k_x = 0$. A flat band is formed by the modes corresponding to the diffraction orders $(m_x = \pm 1, m_y)$, $m_y \in \mathbb{Z}$, near the energy corresponding to the lattice constant a_x . These modes are relatively flat near their vertices and are separated in k_y by the length of the reciprocal lattice vector corresponding to a_y . Thus, increasing the aspect ratio a_y/a_x narrows the width of the Brillouin zone, yielding a flatter band. Because these modes are based on the diffractive orders $m_x = \pm 1$, they lie along the lines $k_x = \pm 2\pi/a_x$ depicted in Fig. 2(b), and thus for a flat band to appear, the structure factor $S(\mathbf{k})$ must take nonzero values densely enough along these lines.

The empty lattice approximation allows us to make five predictions concerning the flat band:

1. The flat band forms at an energy close to the spectral positions of the vertices of the flat-band modes, because the dispersion is the flattest near its vertex. The flat-band energy is determined by the distance of the linelike feature in the structure factor from the line of the observation (here $k_x = 0$). For the rectangular lattice, this distance is determined by the lattice constant a_x via the reciprocal lattice vector \mathbf{b}_1 [see Fig. 2(b)].
2. Because the band structure is repeated, the flat band extends over all values of k_y , i.e., all angles. The size of the Brillouin zone (BZ) in the y direction is inversely proportional to the y period. Taking it to be large, i.e., approaching the limit of a single chain of particles in the x direction, leads to a vanishing BZ thus a denser set of the TM modes and thereby a flatter band. The limit of a single chain of particles in x direction produces a perfectly flat band in k_y , consistent with the absence of any structure in the y direction. However, a single chain would be inefficient in manipulating light over a large area or volume of active material.
3. The flat band is linearly TM polarized near $k_y = 0$; the TE polarization fraction increases away from the Γ point.
4. Because the linelike features formed by the maxima of the structure factor are repeated [Fig. 2(b)], there are flat bands at integer multiples of the energy corresponding to the lattice constant a_x , as will be shown in Section III A.
5. Its diffractive origin confers to the flat band a narrow linewidth—this is confirmed by our experiments.

To verify the feasibility of our flat-band generation strategy, we experimentally test the theoretical predictions in several example cases. The experiments are made with gold nanoparticle arrays, dimensions of the particles in the 100 nm range and of the arrays in the

200x200 square microns range. The samples are fabricated on glass substrates by electron-beam lithography (for more details, see Appendix A). A symmetric refractive index environment ($n = 1.52$) is realized by covering the sample with index-matching oil corresponding to the glass substrate. Dispersions are measured via transmission of white light through the sample, analyzed by Fourier spectrometry, in some cases polarization filtered. More information about the experiments is given in Appendix B. For the case of the rectangular lattice discussed above, the experimentally observed extinction spectrum and the band structure (Fig. 3) calculated using the empty lattice approximation are in excellent agreement. Figure 3(b) shows that the flat band extends between angles of $\pm 17^\circ$, corresponding to the numerical aperture (0.3) of the objective used.

In conclusion, we have demonstrated that lattices whose unit cell is much greater than the lattice constant in one direction exhibit flat bands of diffractive origin in the perpendicular direction. Furthermore, we have argued that flat bands in the band structure are equivalent to linelike features in the structure factor. This makes finding lattice geometries whose structure factors exhibit linelike features a good proxy goal in the search for lattices exhibiting flat bands. However, the simple rectangular lattice offers only two design parameters—one lattice constant to control the energy of the flat band and the other (or the aspect ratio) to control the flatness of the flat band. Moreover, the low density of lattice sites leads to weak light-matter interaction. The lattice also has a flat band in one direction only. Next, we study a category of more complex lattice geometries to alleviate these issues.

III. CHAIN LATTICES

A. Definition and structure factor

We name as a *chain lattice* any lattice whose unit cell consists of N_c chains of N_j lattice sites with constant spacing a_j and with the chain subtending the angle $\theta_j \in [0, \pi)$ with the x axis, where j labels the chains. The chain is translated by $\Delta_j = (\Delta x_j, \Delta y_j)$. The positions of the lattice sites of the j th chain are

$$\left\{ (na_j \cos \theta_j + \Delta x_j, na_j \sin \theta_j + \Delta y_j) \right\}_{n=0}^{N_j-1} \equiv \{n\mathbf{c}_j + \Delta_j\}. \quad (3)$$

Figure 4(a) shows an example of a lattice consisting of two chains. There are now $N_u = \sum_{j=1}^{N_c} N_j$ lattice sites in the unit cell; if there are any overlapping lattice sites between the chains, they must be subtracted from the number of lattice sites in the unit cell N_u and the expression of the structure factor presented below. Hereinafter, we assume that no such sites exist.

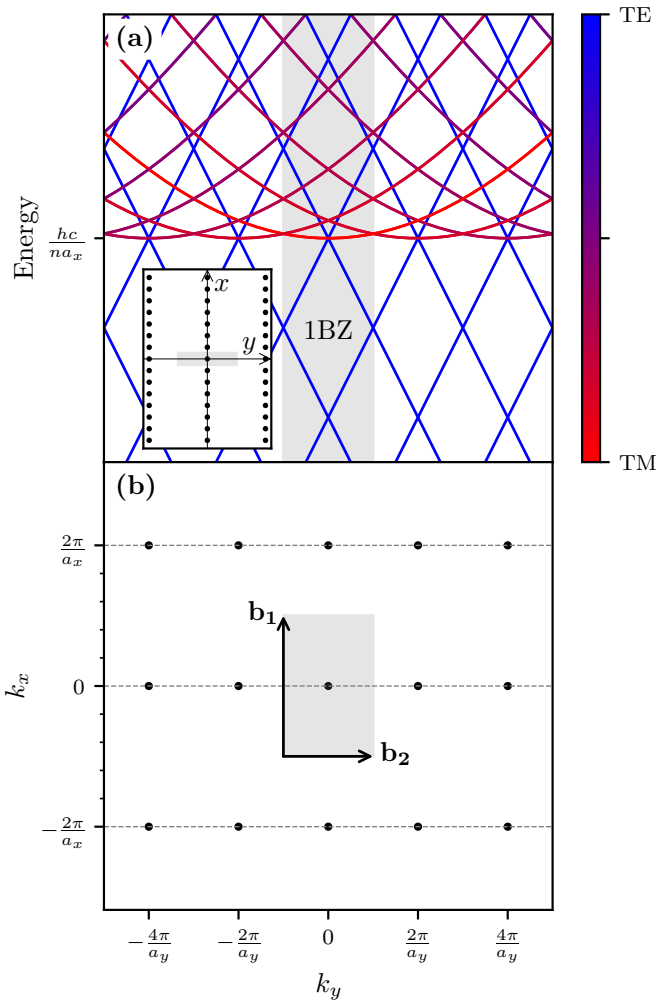


FIG. 2. Band structure (a), and the structure factor in the reciprocal lattice (b), of a rectangular lattice with $a_y = 5a_x$. (a) Flat bands form from the narrowing of the first Brillouin zone (1BZ) in the k_y direction and the repetition of the mainly TM-polarized modes. At larger angles, more TE polarization mixes in. The inset shows the lattice structure and the unit cell shaded in gray. (b) The structure factor $S(\mathbf{k})$ has its maxima (black dots) at the sites of the reciprocal lattice and is zero elsewhere. The gray shaded area indicates the 1BZ; also the reciprocal lattice vectors \mathbf{b}_1 and \mathbf{b}_2 are indicated. The horizontal, gray lines in panel (b) are guides for the eye to highlight the linelike features in the structure factor. The distance between the lines is $|\mathbf{b}_1|$ —this determines the energy of the flat band. Note that the axes in panel (b) are not to scale; the 1BZ is five times wider in the k_x direction than in the k_y direction. The minor ticks on the k_x axis in panel (b) correspond to the width of the 1BZ in the k_y direction.

The structure factor of the complete lattice is

$$\begin{aligned}
 S(\mathbf{k}) &= \frac{1}{N_u^2} \left| \sum_{j=1}^{N_c} \sum_{n=0}^{N_j-1} e^{i\mathbf{k} \cdot (n\mathbf{c}_j + \mathbf{\Delta}_j)} \right|^2 \\
 &= \frac{1}{N_u^2} \left| \sum_{j=1}^{N_c} \underbrace{e^{i\mathbf{k} \cdot \mathbf{\Delta}_j}}_{\equiv \varphi_j(\mathbf{k})} \sum_{n=0}^{N_j-1} \underbrace{[e^{i\mathbf{k} \cdot \mathbf{c}_j}]^n}_{\equiv N_j S_j(\mathbf{k})} \right|^2. \quad (4)
 \end{aligned}$$

Next, we consider the contribution of the j th chain $S_j(\mathbf{k})$. It takes the form of a truncated geometric series and reaches its maximum value (1) when the argument of the exponential is an integer multiple of $2\pi i$, i.e.,

$$\begin{aligned}
 \mathbf{k} \cdot \mathbf{c}_j &= 2\pi l, \quad l \in \mathbb{Z} \\
 \Rightarrow k_y &= \frac{2\pi l}{a_j \sin \theta_j} - (\cot \theta_j) k_x. \quad (5)
 \end{aligned}$$

This equation describes a family of lines in the k_x - k_y plane. Because the partial sum S_j is maximized along these lines, the structure factor has local maxima at the sites of the reciprocal lattice at or close to these lines. Figure 4(b) confirms that the maxima of the structure factor calculated from the definition Eq. (4) [or equivalently, Eq. (1)] for a representative chain lattice appear near the lines defined by Eq. (5). The slope of the family of lines defined by Eq. (5) is $-\cot \theta_j$, which corresponds to the angle

$$\arctan(-\cot \theta_j) = -\frac{\pi}{2} + \theta_j, \quad (6)$$

that is, the flat bands can be observed at right angles to the lattice chains that generate them, consistent with the understanding given by the simple rectangular lattice example in Section II.

It is intuitively clear that the energy of the flat band corresponds to the spacing a_j of the corresponding chain. Here, we show how it can be derived. As established in Section II, in the empty lattice approximation, the flat band is observed at the energy corresponding to the k -space separation of a linelike feature in the structure factor and the observation line [see Fig. 2]. We assume the line of observation to lie along one of the linelike features in the structure factor given in Eq. (5). The energy of the flat bands is then given by the separation of two neighboring lines in the family of lines of Eq. (5). Denoting this distance by κ_j , we compute its value from the expression for the distance of two parallel lines:

$$\kappa_j = \frac{2\pi}{a_j \sin \theta_j} \frac{1}{\sqrt{1 + \cot^2 \theta_j}} = \frac{2\pi}{a_j}. \quad (7)$$

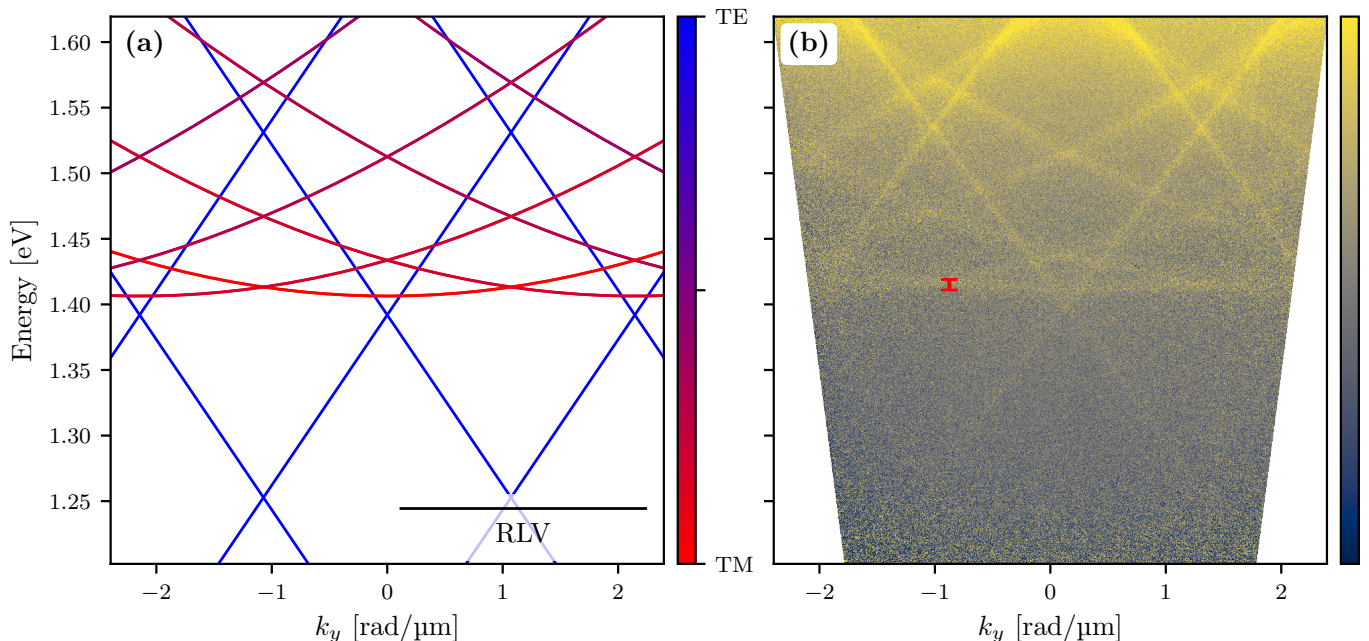


FIG. 3. Calculated band structure [panel (a)] and extinction spectrum [panel (b)] of a rectangular lattice of gold nanoparticles with diameter 110 nm and height 50 nm with lattice constants $a_x = 580$ nm, $a_y = 2930$ nm in an index-symmetric environment with refractive index $n = 1.52$. Sample fabrication (Appendix A) and experimental setup and procedures (Appendix B) are described in the Appendix. The scale bar of panel (a) shows the magnitude of the reciprocal lattice vector (RLV) in the k_y direction. In panel (b), the color scale from blue (minimum) to yellow (maximum) corresponds to extinction averaged over five measurements. The red bar estimates the linewidth of the flat band as 8 meV (5 nm).

Therefore, the flat bands appear at energies

$$E_m = \frac{hc_0}{na_j} m, \quad m \in \mathbb{N}, \quad (8)$$

where h is the Planck constant, c_0 the speed of light in vacuum and n the refractive index of the background medium. This result is evident for lattices where the particle spacing and the size of the unit cell are the same, such as the rectangular lattice of Fig. 2. However, in lattices with multiple lattice sites per unit cell [see Fig. 5], the system is characterized by two distinct periodicities: that of the chain's spacing and that of the unit cell. In the following Sections, we will show that this result arises from the fact that only the diffraction orders corresponding to the chain's spacing contribute to the flat band.

Mathematically speaking, in the limit of large N_j , S_j becomes the Kronecker comb (sum of equispaced delta functions). In Section II, we established creating line-like features in the structure factor as a proxy goal for attaining flat bands. Ideally, the structure factor would take the form of a Kronecker comb. On the other hand, the form of S_j is essentially that of the inverse discrete Fourier transform. The discrete Fourier transform dual of the Kronecker comb is an equispaced sequence, i.e., the chain lattice of Eq. (3). Hence, we conclude that the equispaced chains are a natural way to generate line-like features in the structure factor and flat-band scattering within the purview of the empty lattice approximation.

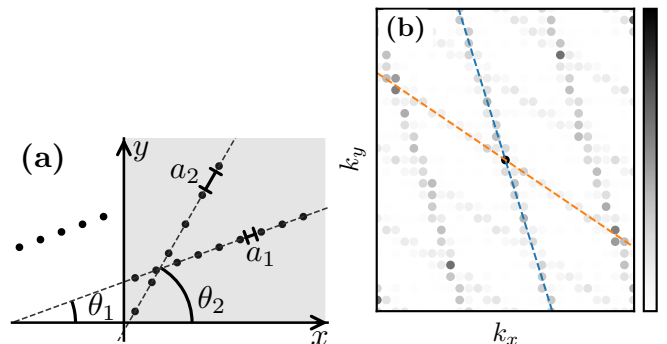


FIG. 4. Panel (a) shows a schematic of a chain lattice consisting of two chains. Lattice sites are indicated by black dots, and the unit cell of the lattice is shaded in gray. The structure factor of the lattice computed from the definition in Eq. (1) is shown in panel (b), with darker color indicating a greater value. The blue and orange lines are the lines defined by Eq. (5) for $l = 0$ for the angles θ_1 and θ_2 .

B. Rectangular chain lattices

As the simplest realization of the chain lattice concept, we now consider chain lattices that consist of two perpendicular chains. Hereafter, we refer to such lattices as *rectangular chain lattices*, and introduce the shorthand notation $N_x \times N_y$, where the first (second) number indicates the number of lattice sites per unit cell in the chain

parallel to the x axis (y axis). The lattice constant of the x -oriented (y -oriented) chain is a_x (a_y). There are $N_u = N_x + N_y - 1$ lattice sites in the unit cell; the -1 is to avoid calculating the lattice site at the origin twice. The lattice vectors and the reciprocal lattice vectors are

$$\begin{aligned} \mathbf{a}_1 &= \begin{pmatrix} N_x a_x \\ 0 \end{pmatrix}, & \mathbf{a}_2 &= \begin{pmatrix} 0 \\ N_y a_y \end{pmatrix}, \\ \mathbf{b}_1 &= \begin{pmatrix} \frac{2\pi}{N_x a_x} \\ 0 \end{pmatrix}, & \mathbf{b}_2 &= \begin{pmatrix} 0 \\ \frac{2\pi}{N_y a_y} \end{pmatrix}. \end{aligned} \quad (9)$$

The structure factor $S(\mathbf{k})$ for this lattice has been derived in Appendix C and at the sites of the reciprocal lattice ($\mathbf{k} = q_1 \mathbf{b}_1 + q_2 \mathbf{b}_2$, $q_1, q_2 \in \mathbb{Z}$) is

$$S(\mathbf{k}) = \begin{cases} 1, & \text{if } q_1 = l_1 N_x \wedge q_2 = l_2 N_y, & (10a) \\ \frac{(N_x - 1)^2}{N_u^2}, & \text{if } q_1 = l_1 N_x \wedge q_2 \neq l_2 N_y, & (10b) \\ \frac{(N_y - 1)^2}{N_u^2}, & \text{if } q_1 \neq l_1 N_x \wedge q_2 = l_2 N_y, & (10c) \\ \frac{1}{N_u^2}, & \text{if } q_1 \neq l_1 N_x \wedge q_2 \neq l_2 N_y, & (10d) \end{cases}$$

where $l_1, l_2 \in \mathbb{Z}$. The structure factor is visualized (for a particular choice of lattice parameters) in the inset of Fig. 5(a). The four cases of Eq. (10) are apparent here: the global maxima [Eq. (10a)] occur at the intersections of the linelike features, and are marked with black in Fig. 5. The secondary maxima Eqs. (10b) and (10c) form horizontal (vertical) linelike features, marked with green (blue) in Fig. 5. At other sites of the reciprocal lattice [Eq. (10d)], the structure factor is negligible; these sites have been marked with orange dots in Fig. 5. The flat band along $k_x = 0$ is formed by modes for which $q_1 = N_x$, i.e., those of Eq. (10b) with $l_1 = \pm 1$. For these modes, the structure factor takes a relatively high value ($S \approx 0.4$ for the lattice of Fig. 5). The dense grid of points in the reciprocal space corresponds to the large supercell, while the sparsely distributed points where the structure factor is strongest are given by the (smaller than unit cell) periods of the chains. This is a general feature of chain lattices with multiple lattice sites in the unit cell: in contrast to the rectangular lattice (with only one lattice site in the unit cell) studied in Section II, now only certain non-TE modes contribute to the flat band.

To corroborate these theoretical findings, we measured the extinction spectrum of a 13x7 rectangular chain lattice of gold nanodisks with lattice constants $a_x = 580$ nm and $a_y = 1160$ nm. The extinction spectrum in TM polarization is shown in Fig. 5 along the corresponding calculated band structure: a prominent flat band is visible at 1.41 eV, confirming the prediction that the flat band is TM polarized. Generally, the experimental and calculated dispersions are in good agreement. The flat band is noticeably stronger than the flat band of a rectangular lattice [Fig. 3(b)]. We attribute this to the use of the

polarization filter, a larger ratio of unit cell size to the lattice constant, and a larger diameter of the nanoparticles. Furthermore, the band is visibly flatter than that of the rectangular array. This is because of the smaller size of the Brillouin zone, i.e., there are more repetitions of the TM modes within the same in-plane wavevector k_y range.

C. Lattices with multiple flat bands

The results of Section III A apply to each constituent chain of a lattice with multiple chains, and therefore we can devise lattice geometries with flat bands at multiple arbitrary energies at the same angle by overlaying two or more parallel chains with appropriate spacings. If we take the orientation of all chains to be the same (to have the flat bands in the same viewing direction), the chains must be offset in space—this is described by the term Δ_j in Eq. (4). The offset in space corresponds to a phase shift in the structure factor. For a single chain, the phase factor does not change the structure factor. For multiple chains, the phase factors combine to reduce the structure factor. We illustrate this by an example: consider a lattice of two chains with orientations $\theta_{1,2}$, spacings $a_{1,2}$ consisting of $N_{1,2}$ lattice sites and offset in space by $\Delta_{1,2}$. Writing out the structure factor [Eq. (4)] for this lattice yields

$$S(\mathbf{k}) = \frac{1}{N_u^2} |N_1 \varphi_1(\mathbf{k}) S_1(\mathbf{k}) + N_2 \varphi_2(\mathbf{k}) S_2(\mathbf{k})|^2. \quad (11)$$

From this equation, we draw the following conclusions: First, small offsets $\Delta_{1,2}$ (so that $\mathbf{k} \cdot \Delta_{1,2} \approx 0$) reduce the weakening effect. Second, both sublattices can contribute to the structure factor only if $S_1(\mathbf{k})$ and $S_2(\mathbf{k})$ are nonzero (to a sufficient extent) for some value of \mathbf{k} . As discussed in Section III A, $S_{1,2}(\mathbf{k})$ is non-negligible only near the points given by Eq. (5). The criterion of Eq. (5) can be met for both chains at the same time at individual intersection points of the lines for arbitrary chains [see Fig. 4(b)]. If, however, both chains have the same orientation and their spacings are the same (or one is an integer multiple of the other), Eq. (5) is fulfilled by both chains along the lines.

We defer further discussion on how to select the offset parameters to Section III D and for now, to demonstrate that the multiple flat band concept is feasible, designed a lattice consisting of three rectangular chain lattices with different lattice constants sharing a common superperiod. Figure 6 shows the experimentally measured TM-polarized extinction spectrum and the calculated dispersion of the lattice embedded in an index-symmetric environment. The simulated and experimental data are in good agreement, the three flat bands appear at the predicted energies. The features are relatively weak, with the structure factor taking values $S \approx 0.05$ (maximum would be one) for the modes constituting the flat bands.

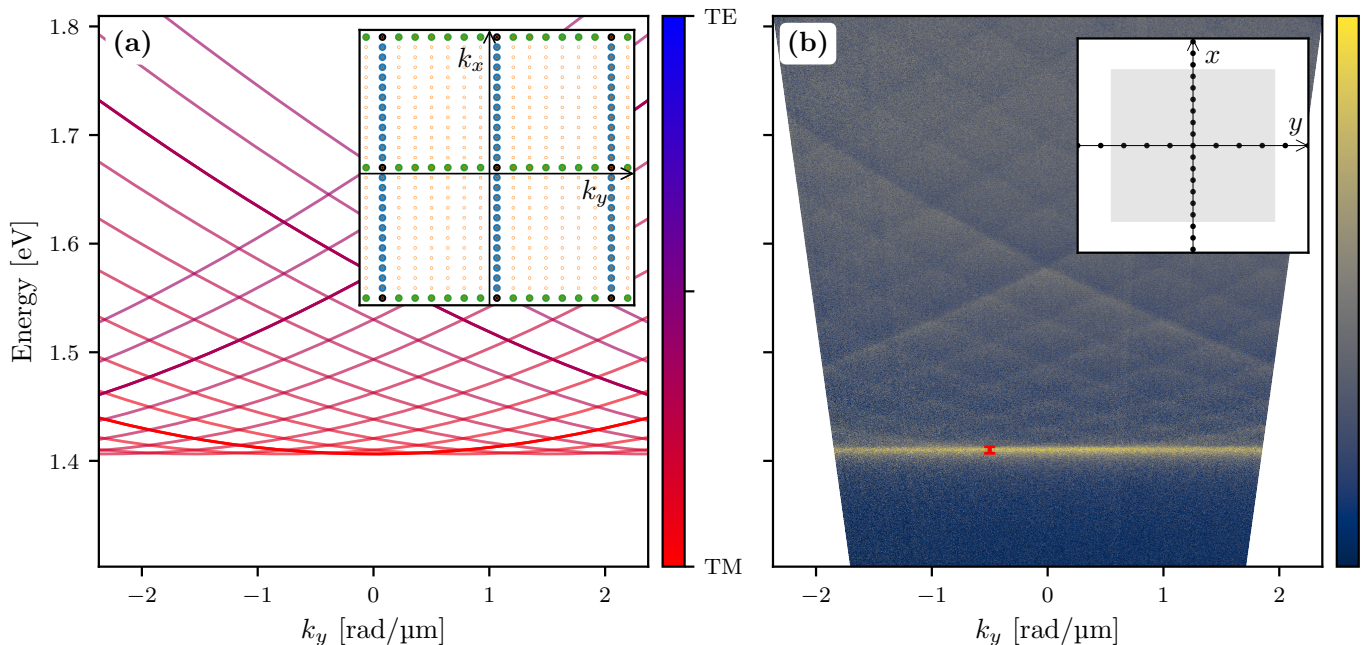


FIG. 5. (a) Calculated dispersion and structure factor (inset) of a $200\ \mu\text{m} \times 200\ \mu\text{m}$ rectangular chain lattice with $N_x = 13$, $a_x = 580\ \text{nm}$, $\theta_x = 0^\circ$ and $N_y = 7$, $a_y = 1160\ \text{nm}$, $\theta_y = 90^\circ$ [see inset in panel (b)] of gold nanocylinders with diameter $130\ \text{nm}$ and height $50\ \text{nm}$ in an index-symmetric background with the refractive index $n = 1.52$. The calculated dispersion only shows modes with the structure factor $S \geq 0.1$ and with TE-polarization fraction $p_{\text{TE}} \leq 0.4$. The color scale of the inset has been explained in the main text. The axes have been slightly displaced for clarity. The flat band is formed by the modes on the top and bottom horizontal rows of peaks (green circles). These modes correspond to the diffraction orders with $q_1 = \pm N_x$ or equivalently, $k_x = \pm 2\pi/a_x$. (b) Experimentally measured extinction spectrum of the same lattice. The extinction spectrum is filtered to show only TM polarization. The linewidth of the flat band indicated by the red bar is $6\ \text{meV}$ ($3.7\ \text{nm}$), corresponding to a Q-factor of 235. In the color bar in (b), yellow denotes maximum and blue minimum extinction.

We conjecture that the flat-band features could be somewhat strengthened by optimizing the offsets of the sublattices, e.g., by maximizing the structure factor of the modes that form the flat bands. However, the maximum value of the structure factor for a chain with N_j lattice sites cannot exceed N_j^2/N_u^2 , where N_u is the total number of lattice sites in the unit cell. For the lattice of Fig. 6, the maximum theoretical values of the structure factor are between 0.10 and 0.13, with the maximum (minimum) obtainable by the chain with the shortest (longest) period.

D. Lattices with duplicated identical chains

In the previous Section, we speculated that the choice of the chain offset parameters can affect the structure factor (strength) of particular modes. To better understand the impact of the offset parameters in rectangular chain lattices, we next compare a rectangular $N \times N$ chain lattice with lattice constant a to a lattice that includes a duplicate of the rectangular chain lattice, displaced by $(\Delta x, \Delta y)$ with respect to the other sublattice. The structure factor of the double rectangular chain lattice $S'(\mathbf{k})$ is related to the structure factor of the single $N \times N$ rectangular chain lattice $S(\mathbf{k})$ via (see Appendix D for the

derivation)

$$S'(q_1 \mathbf{b}_1 + q_2 \mathbf{b}_2) = \cos^2\left(\frac{\pi}{Na}(q_1 \Delta x + q_2 \Delta y)\right) S(q_1 \mathbf{b}_1 + q_2 \mathbf{b}_2), \quad (12)$$

where $q_{1,2}$ are integers and $\mathbf{b}_{1,2}$ the reciprocal lattice vectors. From this, it is evident that the offsets can only weaken the modes of the double rectangular chain lattice compared to the single rectangular chain lattice. Considering the flat band along $k_x = 0$ that is formed by the modes corresponding to the diffraction orders $(q_1, q_2) = (N, m)$, $m \in \mathbb{Z}$ (as explained in Section III B), we can maximize the structure factor of the flat-band modes and minimize it for the TE modes by setting $\Delta x = a$, $\Delta y = \frac{a}{2}$. If N is sufficiently large ($m \ll N$), the structure factors of the flat-band modes (N, m) and the (mainly) TE modes (m, N) are approximately

$$(q_1, q_2) = (N, m) : S' = \cos^2\left[\frac{\pi}{Na}\left(Na + m\frac{a}{2}\right)\right] S \approx S, \quad (13a)$$

$$(q_1, q_2) = (m, N) : S' = \cos^2\left[\frac{\pi}{Na}\left(ma + N\frac{a}{2}\right)\right] S \approx 0. \quad (13b)$$

Physically this means that if one wants to create a strong flat band (high structure factor) from zero up to certain momentum (angle) defined by a certain value of m , then

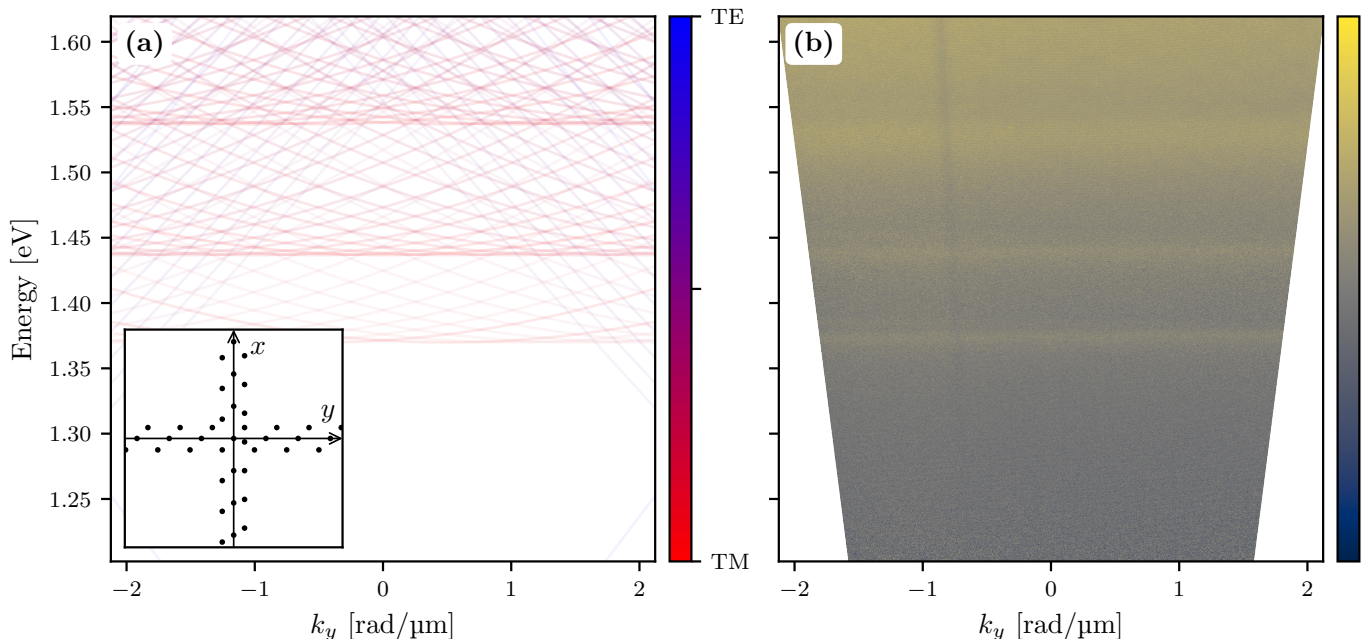


FIG. 6. Calculated band structure of a lattice consisting of three rectangular cross lattices (a) and the experimentally measured extinction spectrum of such a geometry realized by nanoparticles (b). Modes with a higher structure factor are plotted in a more opaque (strong) color. The inset shows a part of the unit cell of the lattice. The lattice comprises superimposed 41×21 , 43×21 , 46×21 rectangular chain lattices with lattice constants $a_x = 592$ nm, 564 nm, 528 nm and $a_y = 592$ nm and offsets $(\Delta x_1, \Delta y_1) = (0$ nm, 0 nm), $(\Delta x_2, \Delta y_2) = (200$ nm, 200 nm), $(\Delta x_3, \Delta y_3) = (-210$ nm, -210 nm). The size of the unit cell was $24.3 \mu\text{m} \times 12.4 \mu\text{m}$. The lattice consisted of gold nanocylinders with a diameter of 120 nm and a height of 50 nm in an environment with the refractive index $n = 1.52$.

N needs to exceed that value. Choosing $\Delta y = \frac{a}{2}$ makes the TE modes near the Γ point vanish. Figure 7(a) shows that the above choice of offsets produces a strong flat band along $k_x = 0$. Conversely, along $k_y = 0$ [Fig. 7(b)], the flat band vanishes near the Γ point, whereas the TE modes appear strong.

E. Chain lattices with a tilted unit cell

Thus far we have studied chain lattices where the orientations of the chains have been parallel to the lattice vectors. Next, we explore lattices where this is no longer the case, starting from a lattice whose unit cell is tilted with respect to the orientation of the chain. In defining such a lattice, there are two issues that must be addressed: selection of the lattice vectors and ensuring that the lattice sites remain within the unit cell.

In proving that chain lattices give rise to flat bands (Section III A), we did not specify the lattice vectors, and thus we can choose the lattice vectors freely, only keeping in mind that the unit cell must be sufficiently larger than the particle spacing to ensure the flatness of the band. To facilitate comparison to the rectangular lattice examined in Section II, we study a chain lattice consisting of one chain of N_u lattice sites with spacing a oriented in the x direction, but with the unit cell of the lattice rotated by an angle α . The lattice vectors \mathbf{a}_1 and

\mathbf{a}_2 and reciprocal lattice vectors \mathbf{b}_1 and \mathbf{b}_2 are thus

$$\begin{aligned} \mathbf{a}_1 &= N_u a \begin{pmatrix} \cos \alpha \\ \sin \alpha \end{pmatrix}, & \mathbf{a}_2 &= N_u a \begin{pmatrix} -\sin \alpha \\ \cos \alpha \end{pmatrix}, \\ \mathbf{b}_1 &= \frac{2\pi}{N_u a} \begin{pmatrix} \cos \alpha \\ \sin \alpha \end{pmatrix}, & \mathbf{b}_2 &= \frac{2\pi}{N_u a} \begin{pmatrix} -\sin \alpha \\ \cos \alpha \end{pmatrix}. \end{aligned} \quad (14)$$

We emphasize that it is not necessary to define the lattice vectors using the chain parameters N_u and a , it is merely a choice of convenience.

As the lattice vectors may be chosen freely, it is possible that some of the lattice sites given by Eq. (3) end up outside the unit cell spanned by the lattice vectors. To address this, an algorithm to ensure that the lattice sites given by Eq. (3) remain in the unit cell while retaining the flat band features for a particular choice of the lattice vectors is presented in Appendix E. The lattices studied in this work have been generated using this algorithm.

To illustrate the effect of rotating the unit cell with respect to the chain orientation, we study a lattice with $N_u = 5$, $\alpha = 2^\circ$, chain orientation $\theta = 0^\circ$ and lattice vectors given by Eq. (14). The lattice geometry is depicted in the inset of Fig. 8(a). The algorithm of Appendix E creates here a chain that appears staggered in the y direction. Despite this, the orientation of the chain is $\theta = 0^\circ$ and it forms a flat band along $k_x = 0$. This is evinced by the calculated band structure of the lattice [Fig. 8(a)], which shows a relatively flat band near the

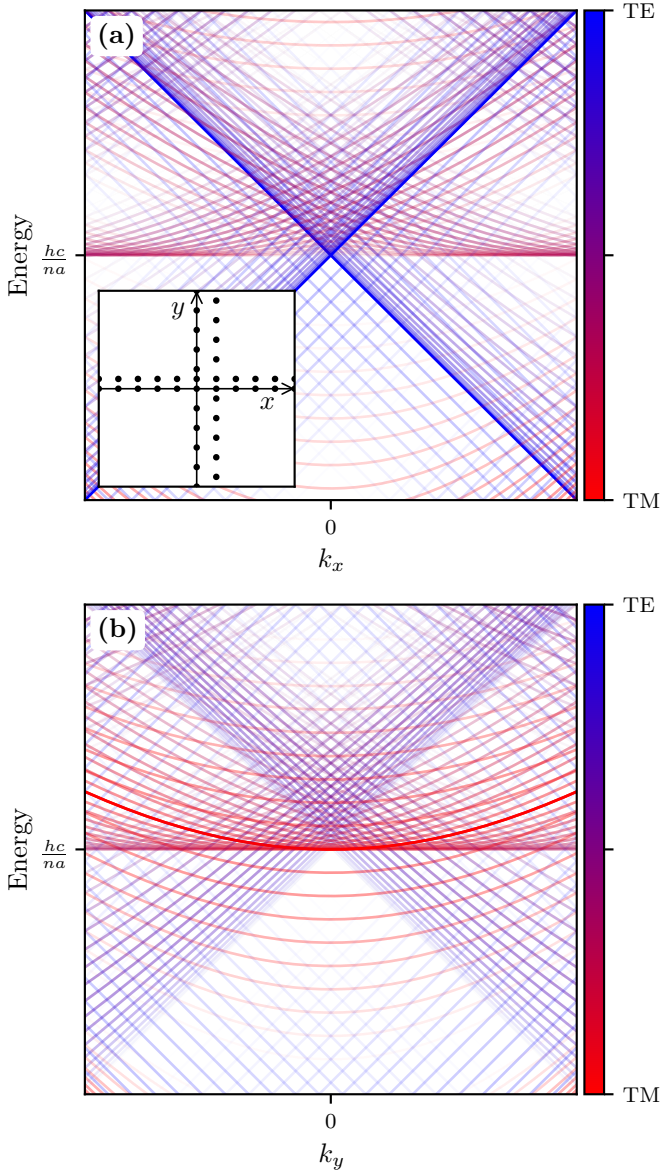


FIG. 7. Calculated dispersions of a double 21×21 rectangular chain lattice with lattice constant a and offsets $\Delta x = a$ and $\Delta y = a/2$ along $k_y = 0$ [panel (a)] and $k_x = 0$ [panel (b)]. Modes with a higher structure factor are plotted in a more opaque (strong) color. The inset of panel (a) shows a part of the unit cell. In determining the polarization of the modes, the plane of incidence is the xz plane in panel (a) and the yz plane in panel (b).

energy corresponding to the chain spacing. By way of similar reasoning as given in Section III B and from the structure factor [Fig. 8(b)], we see that the flat band is formed by the modes $(\pm N_u, m)$, $m \in \mathbb{Z}$.

Despite their similar geometries, the band structures of the rectangular lattice [Fig. 2(a)] and of the chain lattice with the rotated unit cell [Fig. 8(a)] are markedly different: the small angle between the chain and one of the lattice vectors lifts the two-fold degeneracy of the flat-band modes leading to a significant distortion of the flat

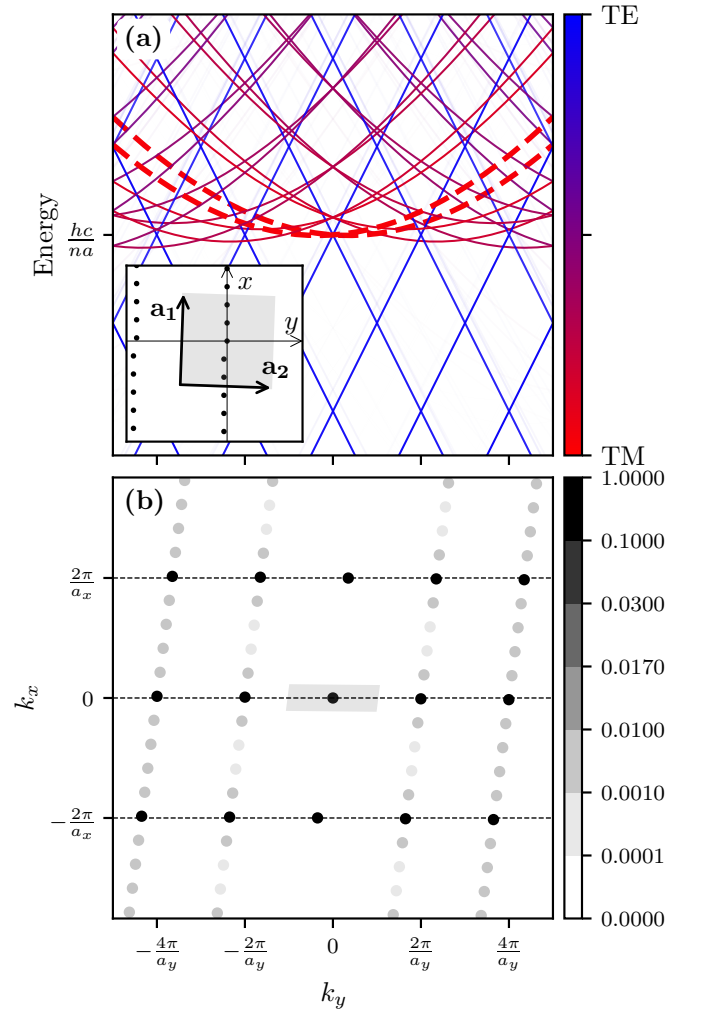


FIG. 8. Band structure [panel (a)] and structure factor [panel (b)] of a chain lattice consisting of one five-site chain in the x direction whose lattice vectors \mathbf{a}_1 and \mathbf{a}_2 are rotated by 2° [see inset in panel (a)]. The two modes highlighted by dashed bold lines in panel (a) are the modes $(\pm 5, 0)$, indicating the lifting of the degeneracy. In panel (b), the shaded area designates the first Brillouin zone and the dashed lines the lines of Eq. (5). The color scale of the structure factor has been chosen to highlight that the modes close to the lines of Eq. (5) are much stronger than any other modes.

band. The lifting of the degeneracy arises from the fact that the reciprocal lattice [Fig. 8(b)] is not symmetric about $k_x = 0$. Furthermore, the lifting of the degeneracy caused the linewidth of the flat band to increase.

We conclude that ensuring that the lines of the peaks of the structure factor given by Eq. (5) intercept sites of the reciprocal lattice is beneficial for the strength and flatness of the flat band. The location of the reciprocal lattice sites, given by the lattice period (unit cell/supercell size) determines where the structure factor can have non-zero values in the first place, whereas the lines of Eq. (5), given by the unit cell structure, determine the locations in the k_x - k_y plane where the structure factor can have

high values—obviously, for a strong flat band, these two should overlap.

F. Triangular chain lattices

We concluded the previous Section by establishing that ideally, the lines of the peaks of the structure factor given by Eq. (5) should intersect the sites of the reciprocal lattice. In the rectangular chain lattices (see Section III B), this was accomplished by aligning the chains with the lattice vectors. Next, by examining a triangular chain lattice, we show that it is possible to add a third chain that aligns with the sites of the reciprocal lattice.

A *triangular chain lattice* consists of three chains with N lattice sites spaced distance a apart at angles 0° , 60° , and 120° to the x axis. The lattice vectors \mathbf{a}_1 and \mathbf{a}_2 and the reciprocal lattice vectors \mathbf{b}_1 and \mathbf{b}_2 of the lattice are

$$\begin{aligned} \mathbf{a}_1 &= \begin{pmatrix} Na \\ 0 \end{pmatrix}, \quad \mathbf{a}_2 = \begin{pmatrix} -\frac{1}{2}Na \\ \frac{\sqrt{3}}{2}Na \end{pmatrix}, \\ \mathbf{b}_1 &= \begin{pmatrix} \frac{2\pi}{Na} \\ \frac{2\pi}{\sqrt{3}Na} \end{pmatrix}, \quad \mathbf{b}_2 = \begin{pmatrix} 0 \\ \frac{4\pi}{\sqrt{3}Na} \end{pmatrix}. \end{aligned} \quad (15)$$

The angles at which the flat bands appear, given by Eq. (6), coincide with the vectors \mathbf{b}_1 , \mathbf{b}_2 and $\mathbf{b}_1 - \mathbf{b}_2$ [see Fig. 9(b)]. Furthermore, in a triangular lattice, $|\mathbf{b}_1| = |\mathbf{b}_2| = |\mathbf{b}_1 - \mathbf{b}_2|$, and therefore, all three flat bands have equally many contributing modes. The theoretical predictions are confirmed by empty lattice calculations [Fig. 9(a)] and experimentally [Fig. 9(c)].

G. Chain lattices with oblique unit cells

Nonorthogonal lattice vectors lift the degeneracy of the flat-band modes, which can be used to increase the flatness of the flat band by choosing the angle between the lattice vectors α such that it distributes the flat-band modes as evenly as possible. For example, lifting the degeneracy of doubly degenerate modes, and then placing them evenly, improves the flatness of the resulting band effectively by a factor of two. Moreover, one of the lattice vectors is aligned with the chain orientation to ensure that the degeneracy is lifted only by translating the modes with respect to the wavevector k_y and not the energy (as was the case for the lattice of Fig. 8). To illustrate, we consider a rectangular lattice with lattice vectors and reciprocal lattice vectors

$$\begin{aligned} \mathbf{a}_1 &= \begin{pmatrix} a_x \\ 0 \end{pmatrix}, & \mathbf{a}_2 &= a_y \begin{pmatrix} \cos \alpha \\ \sin \alpha \end{pmatrix}, \\ \mathbf{b}_1 &= \frac{2\pi}{a_x} \begin{pmatrix} 1 \\ -\cot \alpha \end{pmatrix}, & \mathbf{b}_2 &= \frac{2\pi}{a_y} \begin{pmatrix} 0 \\ \frac{1}{\sin \alpha} \end{pmatrix}, \end{aligned} \quad (16)$$

where we assume $a_y > a_x$ so that there is a flat band along the line $k_x = 0$, i.e., the (first) flat band is formed

by the modes $(\pm 1, q_2)$, $q_2 \in \mathbb{Z}$. Next, to distribute the modes that constitute the flat band maximally equally, we require that the k_y coordinates of the modes related to diffraction orders $(\pm 1, q_2)$, for some value of q_2 (we choose $q_2 = 0$) are separated by a half-integer multiple of the width of the Brillouin zone (y component of \mathbf{b}_2) (the k_y coordinates of the modes are given by the y component of the reciprocal vector \mathbf{b}_1 , as is intuitive from Fig. 10). This yields the following condition for the angle of the lattice vectors α :

$$\begin{aligned} 2(b_1)_y &= \left(j + \frac{1}{2}\right) (b_2)_y \\ \Rightarrow \alpha_j &= \arccos \left[-\left(j + \frac{1}{2}\right) \frac{a_x}{2a_y} \right], \end{aligned} \quad (17)$$

where j is an integer in the interval $\left[-\frac{2a_y}{a_x} - \frac{1}{2}, \frac{2a_y}{a_x} - \frac{1}{2}\right]$. Figure 10 shows the band structure of a lattice with $a_y = 5a_x$ and the angle of the lattice vectors $\alpha = \alpha_0 \approx 87.1^\circ$. Compared to the corresponding rectangular lattice (Fig. 2), there are more nondegenerate modes in a given k_y interval, and thus the band is flatter.

H. Multichain lattices, flat bands with a finite angular extent

In Section III D, we established that adding copies of a chain with the same spacing and angle can only reduce the structure factor. We show here that this provides means to design lattices with flat bands with a desired, finite angular extent. To this end, we next consider a lattice whose unit cell is an $a_x \times a_y$ rectangle that includes N lattice sites at positions $\{(0, \Delta_n)\}$, $n \in [0, \dots, N-1]$. We take $a_y > a_x$ so that there is a flat band along $k_x = 0$.

Using Eq. (1), the structure factor of this lattice can be evaluated to yield

$$S(\mathbf{k}) = \frac{1}{N^2} \left| \sum_{n=0}^{N-1} e^{ik_y \Delta_n} \right|^2. \quad (18)$$

We cannot analytically solve the positions $\{\Delta_n\}$ that yield a given structure factor. To be able to connect the angular extent of the flat band to the design parameters, we select $\Delta_n = \Delta_y n$, where Δ_y is a constant spacing parameter. With this choice, the structure factor $S(\mathbf{k})$ becomes

$$S(\mathbf{k}) = \frac{1}{N^2} \frac{1 - \cos(\Delta_y k_y N)}{1 - \cos(\Delta_y k_y)} \approx 1 - \frac{1}{12} (N^2 - 1) (\Delta_y k_y)^2. \quad (19)$$

The latter approximate value is valid for small values of the arguments of the cosines. The structure factor has a maximum at $k_y = 0$, $S(k_y = 0) = 1$, and its minimal value is zero. Thus from the above Taylor series expression at $k_y = 0$, we can solve for the value of k_y corresponding to half-width at half-maximum k_{HWHM}

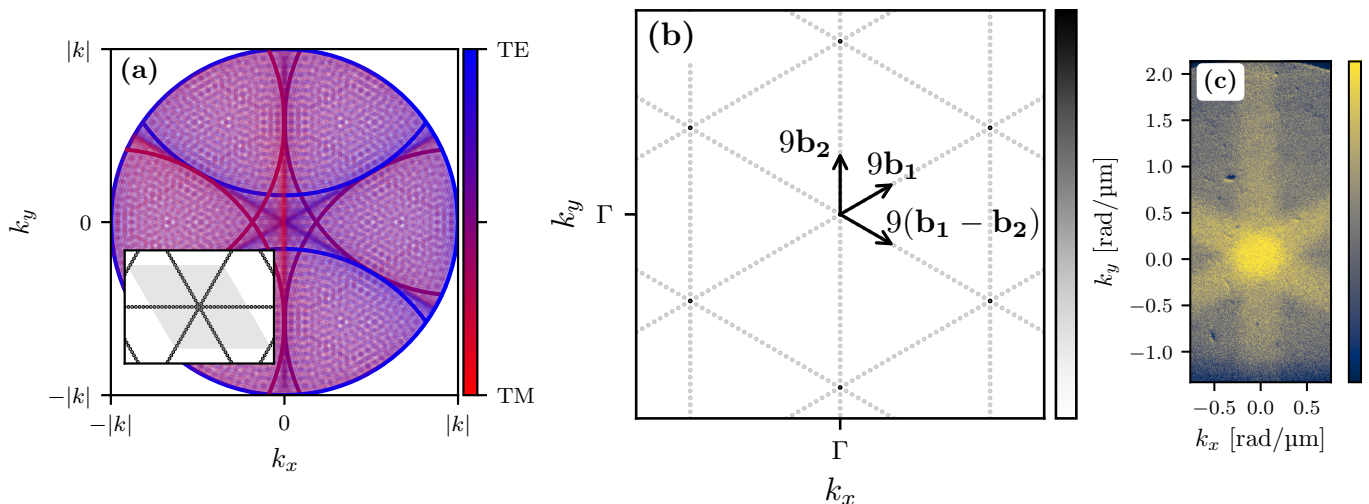


FIG. 9. Calculated band structure at the energy corresponding to the lattice constant [panel (a)], structure factor [panel (b)] and extinction spectrum viewed through a filter with central wavelength of 880 ± 5 nm [panel (c)] of a triangular chain lattice with $N = 25$ and $a = 570$ nm in a background with refractive index $n = 1.52$. Inset of panel (a) shows a part of the lattice, with the unit cell shaded in gray. The reciprocal lattice vectors \mathbf{b}_1 and \mathbf{b}_2 and the difference $\mathbf{b}_1 - \mathbf{b}_2$ are aligned with the lines of the peaks of the structure factor. The strength (color) of the peaks and the length of the vectors are exaggerated for ease of viewing. The extinction spectrum shows three flat bands at the predicted angles. The lattice consisted of gold nanocylinders with a diameter of 150 nm and a height of 50 nm. In the color scale of panel (c), yellow (blue) corresponds to maximum (minimum) extinction.

($S(k_{\text{HWHM}}) = 0.5$):

$$k_{\text{HWHM}} = \frac{\sqrt{6}}{\Delta_y \sqrt{N^2 - 1}}. \quad (20)$$

This value approximately characterizes the extent of the flat band in momentum. Intuitively one can understand this effect as destructive interference caused by the multiple particles in the unit cell. However, for small k_y the corresponding length scale (effective wavelength) is large compared to the spacing between the particles, and even the total length $N\Delta_y$, thus this effectively subwavelength feature does not cause a major effect, and one still has a flat band over small values of k_y .

At the energy of the flat band [which is determined by a_x per Eq. (8)], the corresponding angle θ_{HA} is

$$\theta_{\text{HA}} = \arcsin\left(\frac{k_{\text{HWHM}}}{k_0}\right) = \arcsin\left(\frac{a_x}{2\pi\Delta_y} \sqrt{\frac{6}{N^2 - 1}}\right). \quad (21)$$

Finally, to design a lattice with a given angular range θ_{HA} , we solve for the y -offset magnitude Δ_y :

$$\Delta_y = \frac{a_x}{\pi \sin \theta_{\text{HA}}} \sqrt{\frac{3}{2(N^2 - 1)}}. \quad (22)$$

Notably, the lattice constant a_y does not directly appear in the expression for Δ_y . However, it controls how many modes appear within the angular range determined by the half-angle θ_{HA} .

To verify the above predictions, Fig. 11 shows the band

structure of a lattice designed to have a flat band extending to $\theta_{\text{HA}} = 15^\circ$. As expected, the modes whose vertices are at k_y values corresponding to angles greater than 15° appear weak.

I. Summary of the results

We have studied several examples of chain lattices, and now summarize the results as the following design rules for creating lattices exhibiting flat bands:

1. A 1D chain of lattice sites with constant spacing a_j subtending an angle θ_j with the x axis gives rise to a flat band that is observable perpendicular to the angle θ_j and at wavelength na_j , where n is the refractive index of the background medium. If multiple chains with different spacing or orientation are overlaid in the same lattice, multiple flat bands appear.
2. The contribution of the j th chain [captured in the partial sum S_j of Eq. (4)] to the structure factor S is proportional to the number of lattice sites in the chain N_j^2 , while the structure factor is normalized by the number of lattice sites in the unit cell N_u^2 . Thus, the distribution of the lattice sites to different chains can be used to control the relative strengths of the modes pertaining to each chain.
3. If multiple copies of a chain with the same periodicity, but spatially offset by Δ_j , are added into a lattice, the effect of the offsets Δ_j is to weaken the

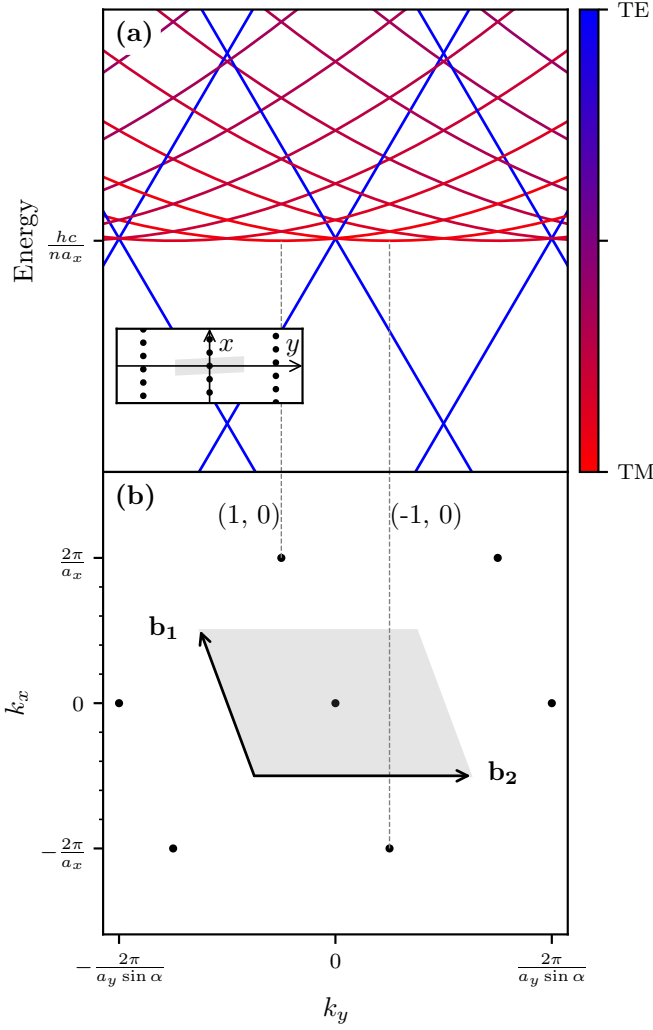


FIG. 10. Band structure [panel (a)] and structure factor [panel (b)] of a lattice with lattice vectors given by Eq. (16) with $a_y = 5a_x$ and $\alpha = \alpha_0$ [Eq. (17)]. The inset of panel (a) shows the real lattice with the unit cell shaded in gray. The shaded area in panel (b) depicts the first Brillouin zone. The flat-band modes closest to the Γ point ($\pm 1, 0$) are indicated in both panels.

modes at the crossings of the k -space lines originating from the chains j and $j' \neq j$, i.e., modes common to the chains j and j' ; this effect is captured in the term $\varphi_j(\mathbf{k})$ in Eq. (4). The weakening effect is the most severe for parallel chains because it applies to all modes.

4. In the optimal case, the lines of the peaks of the structure factor defined by Eq. (5) intersect the sites of the reciprocal lattice. The effect of the misalignment between the lines of the peaks of the structure factor and the sites of the reciprocal lattice on the quality of the flat band can be reduced by increasing the density of the modes, i.e., by increasing the size of the unit cell in real space.

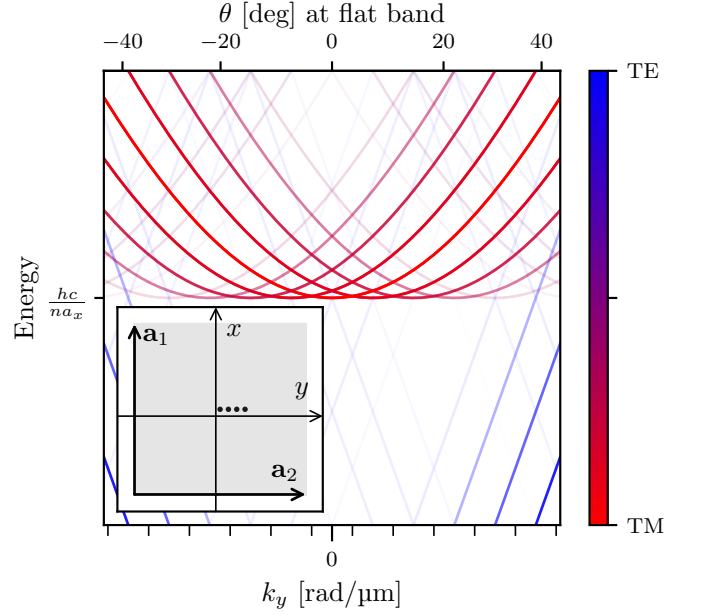


FIG. 11. Band structure of a lattice designed to have a flat band between $\pm 15^\circ$. The inset shows the unit cell (in gray) of the lattice, which has four particles, with spacing of $\Delta_y \approx 0.389a_x$ [calculated using Eq. (22)]. Note that the inset is not to scale, $a_y = |\mathbf{a}_2| = 8a_x$ ($a_x = |\mathbf{a}_1|$); this value of a_y was selected to best visualize the weakening of the flat band at greater angles. The axes in the inset have been slightly displaced for ease of viewing, the leftmost lattice site is actually at the origin. The spacing of the minor ticks of the k_y axis corresponds to the width of the Brillouin zone.

5. Nonorthogonal lattice vectors can be used to lift the degeneracy of the modes that form the flat band. This can be used to increase the flatness of the band by selecting the angle of the lattice vectors using Eq. (17).
6. Flat bands arising from chain lattices naturally extend over all angles. Lattices yielding flat bands with a finite angular range can be designed by adding multiple copies of the same chain, offset by a constant step selected using Eq. (22).

IV. CONCLUSIONS AND DISCUSSION

We have theoretically formulated and experimentally demonstrated a strategy to create flat bands of diffractive origin by lattices where the width of the unit cell in one direction is large compared to the lattice site spacing in the perpendicular direction. These flat bands naturally extend over all angles, but can be tailored to cover only a finite angular range if desired. The flat bands are dominantly TM polarized at small angles. We introduced a category of lattice geometries, the chain lattices, and showed that, using equispaced 1D chains of lattice sites as building blocks, superlattice geometries can be engi-

neered to host flat bands at energies and angles that are determined by the geometry of the sublattice chain via simple analytical relations. Intuitively, one can conclude that a single 1D chain exhibits a flat band in the direction perpendicular to the chain because of lack of structure in that direction, while the periodicity of the chain in the other direction allows selecting a specified, narrow value for the energy of the band. The flat-band design method was demonstrated by several representative examples, and in each case the theoretical predictions matched well with experimental Fourier spectroscopy data from lattices of gold nanocylinders fabricated by electron-beam lithography. Because of their purely diffractive origin, we expect the flat bands to also appear in various other lattices of scatterers, e.g., arrays of dielectric nanoparticles where the absence of ohmic losses would help achieving even higher-quality modes.

1D chains of nanoparticles have been investigated in Ref. [61], and the authors reported flat-band lasing. Our work complements this observation by providing a theoretical explanation for the appearance of the flat band. Superlattice geometries (where the particle spacing is small compared to the size of the unit cell) have previously been investigated [62–64], but in those studies, the square geometry of the sublattice excludes flat bands. While asymmetric, two-dimensional rectangular arrays have previously been employed to realize flat bands [49, 50], in those systems the band flattening arises from coupling of guided modes or refractive index contrast with the environment. In contrast, the flat bands reported here originate from diffraction. Moreover, chain lattices do not require fine-tuning of the rectangular aspect ratio to achieve band flattening, relaxing the geometric constraints inherent to previously reported implementations. In another realization, a lattice of crossing dielectric waveguides—similar in appearance to the rectangular chain lattices introduced in this work—was observed to feature bidirectional flat bands [52], however the underlying physical mechanism is based on combining a metasurface–waveguide with features of tight-binding systems, which is very different from our diffraction-originated flat bands.

Previous realizations of flat bands in photonic systems have relied on (i) limiting the range of coupling using arrays of parallel waveguides [4, 25–29], photonic moiré lattices [2, 36–39], coupled metallic resonators [30–32] or short-lived exciton-polaritons [33–35], (ii) using gratings to couple free space modes to waveguided modes [6, 7, 45–49, 51, 52], (iii) using strain to flatten the Landau levels [42], (iv) exploiting the rotational degrees of freedom of the constituent elements of the unit cell [44], or (v) band folding arising from large superlattice periodicity and disorder-induced qBICs [43]. The flat bands investigated here arise purely from diffraction, through the superposition of TM modes that are relatively flat near their vertices. One of the advantages of this approach is that the flat bands naturally extend over all angles, whereas the flat bands arising from coupling to wave-

guide modes, for example, have a limited angular range, and the moiré bands are only approximately flat and only for precise conditions.

The SLRs of arrays of plasmonic nanoparticles have been used to enhance and control the emission of organic dye molecules [65], OLEDs [66–68], and LEDs [69, 70]. For these applications—and for other potential applications such as increasing absorption in photodetectors or photovoltaics—the chromatic dispersion of SLRs of simple lattice geometries is usually an unwanted effect. The lattice geometries presented in this work offer means to enhance emission or absorption at a narrow energy range over all or desired angles. In particular, lattices featuring flat bands at multiple target energies are interesting for white-light generation or absorption. Furthermore, the flat bands being linearly TM polarized may be beneficial to applications requiring polarized light. Lattices yielding flat bands with a finite, tunable angular range may be useful, e.g., in OLEDs, where the range could be matched with the range of angles (k_{\parallel} values) that is allowed to outcouple before total internal reflection at higher angles.

In designing the chain lattices, there is an ineluctable tradeoff: while a larger unit cell produces a flatter band, it also leads to a reduced filling factor, thus weakening the light–matter interaction. Despite this, the experimental data presented here show that designing lattice geometries with visibly flat bands is feasible. Furthermore, we showed that the band flatness can be increased by a suitable choice of the angle of the lattice vectors. Flat-band lasing has been reported from photonic moiré lattices [35, 40, 41] and metasurface-on-a-waveguide structures [49]. The lattice geometries proposed here offer an exciting platform for plasmonic flat-band lasing and amplified spontaneous emission; experimental results on those topics are presented in Ref. [71]. Other potential applications include slow-light devices and enhancing nonlinear optical processes, such as harmonic generation. As our strategy for creating flat bands relies on simple generic principles expressed by analytical formulas, in contrast to numerical approaches, it can be easily adapted to different systems and applications.

COMPETING INTERESTS

R. H., J. L., A. J. J. D., and P. T. declare that they are inventors in a filed PCT (PCT/FI2026/050087) patent application related to the work described in this manuscript. The remaining authors declare no competing interests.

ACKNOWLEDGMENTS

Funded by the European Union. Views and opinions expressed are however those of the author(s) only and do not necessarily reflect those of the European Union or

the European Innovation Council and the SMEs Executive Agency (EISMEA). Neither the European Union nor the granting authority can be held responsible for them (SCOLED, Grant Agreement No. 101098813). This work is part of the Finnish Centre of Excellence in Quantum Materials (QMAT).

The research was performed at the Micronova Nanofabrication Centre of Aalto University.

Appendix A: Sample fabrication

The nanoparticle arrays are fabricated using electron-beam lithography (EBL). For this, a resist (350 μl PMMA A4) is spin-coated onto a 25 mm x 75 mm x 1 mm large borosilicate substrate for 1 minute at 3000 rpm, followed by a 2-minute bake at 175°C on a hot plate. To create a conductive and reflective surface for the lithography process, a 15 nm-thick layer of aluminum is evaporated onto the sample using electron-beam evaporation. After exposure at the EBL, the aluminum layer is etched for 1 min in a 1:1 mixture of AZ351B-developer and DI-water, followed by a 30 s bath in pure DI-water. The resist is developed for 15 s in a 3:1 mixture of isopropanol:MIBK (Methyl isobutyl ketone) followed by a 30 s bath in pure isopropanol. Following the development, 2 nm of titanium and 50 nm of gold are evaporated onto the sample using electron beam evaporation. The excess material is removed in a lift-off process by immersing the sample overnight in acetone.

For the measurements, the arrays are immersed in index-matching oil, and the sample is sealed with a 25 mm x 25 mm x 0.1 mm borosilicate cover slip, to ensure that the arrays are in an index-symmetric environment with a refractive index of 1.52.

Appendix B: Experimental setup

The sample is illuminated with a transmission light source producing diffused white light. The objective (NA 0.3) is used to image the arrays. The back focal plane of the objective is guided to the entrance slit of the spectrometer. The back focal plane of the objective corresponds to the momentum space and hence contains information about the angular properties of the light transmitted through the sample. In the spectrometer, the white light is separated into different wavelengths with a grating and guided to a charge-coupled device (CCD) camera, which records the angle- and wavelength-resolved images. Optionally, a polarizer can be added to the path. A real-space camera is used to record the real-space of the sample and to bring the sample into the focal point of the objective. A real-space iris is used to restrict the light to only the area that is covered by a nanoparticle array. The transmission through the sample T_{array} is

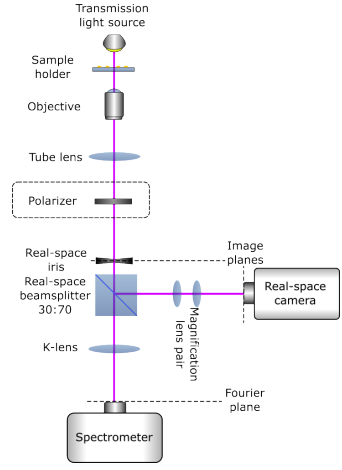


FIG. 12. Schematic of the Fourier imaging setup.

calculated in a post-processing step by

$$T_{\text{array}} = \frac{I_{\text{array}} - I_{\text{background}}}{I_{\text{reference}} - I_{\text{background}}}, \quad (\text{B1})$$

where I_{array} is the intensity recorded in the CCD camera of the spectrometer through the array, $I_{\text{background}}$ is the intensity of the background radiation which is collected by blocking the direct beam path to the spectrometer, and $I_{\text{reference}}$ is the intensity through the sample with no array present, i.e., through the substrate, index-matching oil and cover slip layers. Extinction, shown in the pictures of the main text, is obtained as $1 - T_{\text{array}}$.

Appendix C: Structure factor of a rectangular chain lattice

The positions of the lattice sites in an $N_x \times N_y$ rectangular chain lattice with the lattice constants a_x and a_y are

$$\left\{ (na_x, 0) \right\}_{n=0}^{N_x-1} \cup \left\{ (0, na_y) \right\}_{n=0}^{N_y-1}, \quad (\text{C1})$$

where \cup indicates a union of two sets. There are $N_u = N_x + N_y - 1$ lattice sites in the unit cell; the -1 appears to avoid counting the lattice site at the origin twice. The lattice vectors and the reciprocal lattice vectors are given by Eq. (9). Inserting the positions of the lattice sites to the definition of the structure factor [Eq. (1)] yields

$$S(\mathbf{k}) = \frac{1}{N_u} \left| -1 + \sum_{n=0}^{N_x-1} e^{ik_x na_x} + \sum_{n=0}^{N_y-1} e^{ik_y na_y} \right|^2, \quad (\text{C2})$$

where the -1 again appears to avoid double-counting the lattice site at the origin. Per Section II, the structure factor can have non-zero values only at the sites of the reciprocal lattice, i.e., $\mathbf{k} = q_1 \mathbf{b}_1 + q_2 \mathbf{b}_2$ with $q_1, q_2 \in \mathbb{Z}$.

The geometric sums in Eq. (C2) then evaluate to

$$\begin{aligned} \sum_{n=0}^{N_x-1} e^{ik_x n a_x} &= \sum_{n=0}^{N_x-1} e^{2\pi i q_1 \frac{n}{N_x}} \\ &= \begin{cases} N_x, & \text{if } q_1 = l_1 N_x, l_1 \in \mathbb{Z}, \\ 0, & \text{else.} \end{cases} \end{aligned} \quad (\text{C3})$$

Evaluating the other sum in a similar manner, we obtain the expression for the structure factor

$$S(q_1 \mathbf{b}_1 + q_2 \mathbf{b}_2) = \begin{cases} 1, & \text{if } q_1 = l_1 N_x \wedge q_2 = l_2 N_y, \\ \frac{(N_x-1)^2}{N_u^2}, & \text{if } q_1 = l_1 N_x \wedge q_2 \neq l_2 N_y, \\ \frac{(N_y-1)^2}{N_u^2}, & \text{if } q_1 \neq l_1 N_x \wedge q_2 = l_2 N_y, \\ \frac{1}{N_u^2}, & \text{if } q_1 \neq l_1 N_x \wedge q_2 \neq l_2 N_y, \end{cases} \quad (\text{C4})$$

where $l_1, l_2 \in \mathbb{Z}$.

Appendix D: Structure factor of a symmetric double rectangular chain lattice

We consider a lattice with the (reciprocal) lattice vectors

$$\begin{aligned} \mathbf{a}_1 &= \begin{pmatrix} Na \\ 0 \end{pmatrix}, \quad \mathbf{a}_2 = \begin{pmatrix} 0 \\ Na \end{pmatrix}, \\ \mathbf{b}_1 &= \begin{pmatrix} \frac{2\pi}{Na} \\ 0 \end{pmatrix}, \quad \mathbf{b}_2 = \begin{pmatrix} 0 \\ \frac{2\pi}{Na} \end{pmatrix}, \end{aligned} \quad (\text{D1})$$

with two $N \times N$ rectangular chain lattices with relative displacement $(\Delta x, \Delta y)$ [see inset of Fig. 7(a) in the main text]. The unit cell has $N'_u = 4N - 2$ lattice sites in the unit cell (-2 is to avoid double-counting the sites at the centers of both crosses). To highlight the effect of adding the second pair of chains and the choice of the offset parameters $(\Delta x, \Delta y)$, we compare the structure factor of the double rectangular chain lattice to that of a single rectangular chain lattice, which was calculated in Appendix C. We denote the structure factor of the single rectangular chain lattice by $S(\mathbf{k})$ and that of the double rectangular chain lattice by $S'(\mathbf{k})$. Noting that the double rectangular chain lattice has twice as many lattice sites in the unit cell as the single rectangular chain lattice ($N'_u = 2N_u$), we compute the structure factor $S'(\mathbf{k})$ by inserting the positions of the lattice sites in the

definition of the structure factor [Eq. (1)]:

$$\begin{aligned} S'(\mathbf{k}) &= \frac{1}{N'^2_u} \left| \sum_{n=0}^{N-1} [e^{ik_x n a} + e^{ik_y n a} + \right. \\ &\quad \left. \overbrace{e^{i(k_x \Delta x + k_y \Delta y)}}{\equiv \varphi(\mathbf{k})} (e^{ik_x n a} + e^{ik_y n a})] - 2 \right|^2 \\ &= \frac{1}{4N_u^2} \left| [1 + \varphi(\mathbf{k})] \sum_{n=0}^{N-1} [e^{ik_x n a} + e^{ik_y n a}] - 2 \right|^2 \\ &= \frac{|1 + \varphi(\mathbf{k})|^2}{4} \frac{1}{N_u^2} \left| \sum_{n=0}^{N-1} [e^{ik_x n a} + e^{ik_y n a}] - 2 \right|^2 \\ &= \frac{|1 + \varphi(\mathbf{k})|^2}{4} S(\mathbf{k}). \end{aligned} \quad (\text{D2})$$

Recalling that S can take nonzero values only at the sites of the reciprocal lattice $\mathbf{k} = q_1 \mathbf{b}_1 + q_2 \mathbf{b}_2$, we can write

$$\frac{|1 + \varphi(q_1 \mathbf{b}_1 + q_2 \mathbf{b}_2)|^2}{4} = \cos^2 \left[\frac{\pi}{Na} (q_1 \Delta x + q_2 \Delta y) \right]. \quad (\text{D3})$$

Appendix E: Generation of chain lattices

In generating the coordinates of the lattice sites per Eq. (3), some of the lattice sites may end up outside the unit cell defined by the lattice vectors $\mathbf{a}_{1,2}$. Any lattice sites outside the unit cell must be translated back into the unit cell in a manner that does not affect their contribution to the structure factor. To this end, we note that the structure factor [Eq. (1)] is invariant under a translation of a lattice site by an integer multiple of the lattice vectors. Thus, the steps of the algorithm are simply:

1. Generate the coordinates in the global xy -coordinate system using Eq. (3).
2. Write the coordinates in the basis of the lattice vectors $\mathbf{a}_{1,2}$.
3. Discard the integer part of the coordinates, keeping only the fractional part.

For step 2, we denote the coordinates of the j th lattice site in the basis of the lattice vectors by $\tilde{\mathbf{c}}_j$. They are given by the coordinate transformation

$$\begin{pmatrix} \tilde{c}_{j1} \\ \tilde{c}_{j2} \end{pmatrix} = A^{-1} \left[n \begin{pmatrix} c_{jx} \\ c_{jy} \end{pmatrix} + \begin{pmatrix} \Delta x_j \\ \Delta y_j \end{pmatrix} \right], \quad (\text{E1})$$

where A is the matrix whose columns are the lattice vectors. Because $\mathbf{a}_i \cdot \mathbf{b}_j = 2\pi \delta_{ij}$, where $\mathbf{b}_{1,2}$ are the reciprocal

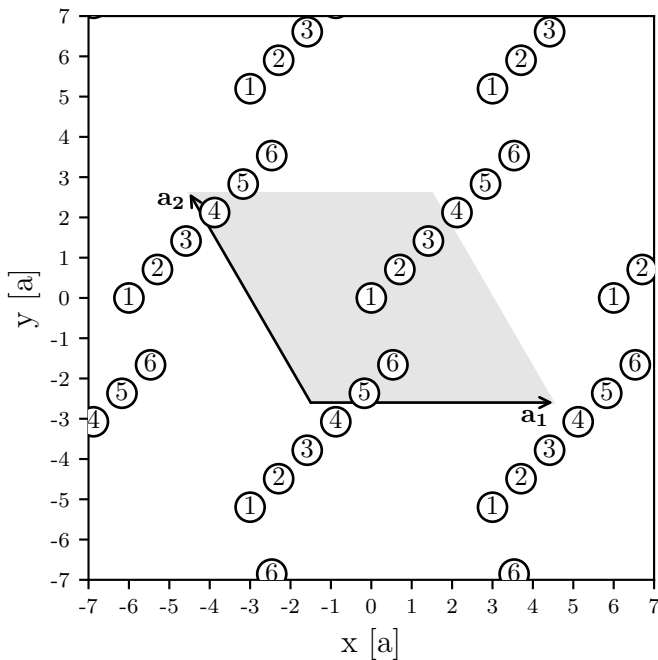


FIG. 13. Illustration of the chain lattice generation algorithm. The depicted lattice consists of one chain with $N = 6$ sites, spacing of a , and orientation $\theta = 45^\circ$. The lattice vectors are $\mathbf{a}_1 = (Na, 0)^T$ and $\mathbf{a}_2 = Na(\cos 120^\circ, \sin 120^\circ)^T$. All sites marked with the same number are related to one another by a translation of an integer multiple of the lattice vectors.

lattice vectors, it follows that

$$A^{-1} = \frac{1}{2\pi} B^T = \frac{1}{2\pi} \begin{pmatrix} b_{1x} & b_{1y} \\ b_{2x} & b_{2y} \end{pmatrix}, \quad (\text{E2})$$

where B is a matrix whose columns are the reciprocal lattice vectors.

Step 3 is accomplished by the replacement $\tilde{\mathbf{c}}_j \rightarrow \tilde{\mathbf{c}}_j - \lfloor \tilde{\mathbf{c}}_j \rfloor$, where $\lfloor \cdot \rfloor$ denotes element-wise rounding down. Here, "rounding down" for negative numbers means rounding away from zero (e.g., $\lfloor -2.2 \rfloor = -3$)—this choice ensures that the coordinates are always in the range $[0, 1)$. Figure 13 illustrates the output of this algorithm.

-
- [1] K. Sun, K. Wang, W. Wang, Y. Cai, L. Huang, A. Alù, and Z. Han, High-Q photonic flat-band resonances for enhancing third-harmonic generation in all-dielectric metasurfaces, *Newton* **1**, 100057 (2025).
- [2] T. Ning, L. Zhao, Y. Huo, Y. Cai, and Y. Ren, Giant enhancement of second harmonic generation from monolayer 2D materials placed on photonic moiré superlattice, *Nanophotonics* **12**, 4009 (2023).
- [3] T. Baba, Slow light in photonic crystals, *Nature Photonics* **2**, 465 (2008).
- [4] R. A. Vicencio, C. Cantillano, L. Morales-Inostroza, B. Real, C. Mejía-Cortés, S. Weimann, A. Szameit, and M. I. Molina, Observation of localized states in Lieb photonic lattices, *Physical Review Letters* **114**, 245503 (2015).
- [5] E. M. Purcell, Proceedings of the American Physical Society: Spontaneous emission probabilities at radio frequencies (1946).
- [6] C. Munley, A. Manna, D. Sharp, M. Choi, H. A. Nguyen, B. M. Cossairt, M. Li, A. W. Barnard, and A. Majumdar, Visible wavelength flatband in a gallium phosphide metasurface, *ACS Photonics* **10**, 2456 (2023).
- [7] M. Choi, C. Munley, J. E. Froch, R. Chen, and A. Majumdar, Nonlocal, flat-band meta-optics for monolithic, high-efficiency, compact photodetectors, *Nano Letters* **24**, 3150 (2024).
- [8] D. Leykam, A. Andreanov, and S. Flach, Artificial flat band systems: from lattice models to experiments, *Advances in Physics: X* **3**, 1473052 (2018).
- [9] D. Leykam and S. Flach, Perspective: photonic flatbands, *Apl Photonics* **3** (2018).
- [10] C. Danieli, A. Andreanov, D. Leykam, and S. Flach, Flat band fine-tuning and its photonic applications, *Nanophotonics* **13**, 3925 (2024).
- [11] M. Kohmoto and B. Sutherland, Electronic states on a Penrose lattice, *Physical Review Letters* **56**, 2740 (1986).
- [12] B. Sutherland, Localization of electronic wave functions due to local topology, *Physical Review B* **34**, 5208 (1986).
- [13] E. H. Lieb, Two theorems on the Hubbard model, *Physical Review Letters* **62**, 1201 (1989).
- [14] A. Mielke, Ferromagnetism in the Hubbard model on line graphs and further considerations, *Journal of Physics A: Mathematical and General* **24**, 3311 (1991).
- [15] H. Tasaki, From Nagaoka's ferromagnetism to flat-band ferromagnetism and beyond: An introduction to ferromagnetism in the Hubbard model, *Progress of Theoretical Physics* **99**, 489 (1998).
- [16] W. Maimaiti, A. Andreanov, H. C. Park, O. Gendelman, and S. Flach, Compact localized states and flat-band generators in one dimension, *Physical Review B* **95**, 115135 (2017).
- [17] W. Maimaiti, S. Flach, and A. Andreanov, Universal d=1 flat band generator from compact localized states, *Physical Review B* **99**, 125129 (2019).
- [18] W. Maimaiti, A. Andreanov, and S. Flach, Flat-band generator in two dimensions, *Physical Review B* **103**, 165116 (2021).
- [19] Y. Cao, V. Fatemi, S. Fang, K. Watanabe, T. Taniguchi,

- E. Kaxiras, and P. Jarillo-Herrero, Unconventional superconductivity in magic-angle graphene superlattices, *Nature* **556**, 43 (2018).
- [20] Y. Cao, V. Fatemi, A. Demir, S. Fang, S. L. Tomarken, J. Y. Luo, J. D. Sanchez-Yamagishi, K. Watanabe, T. Taniguchi, E. Kaxiras, R. C. Ashoori, and P. Jarillo-Herrero, Correlated insulator behaviour at half-filling in magic-angle graphene superlattices, *Nature* **556**, 80 (2018).
- [21] L. Balents, C. R. Dean, D. K. Efetov, and A. F. Young, Superconductivity and strong correlations in moiré flat bands, *Nature Physics* **16**, 725 (2020).
- [22] D. M. Kennes, M. Claassen, L. Xian, A. Georges, A. J. Millis, J. Hone, C. R. Dean, D. N. Basov, A. N. Pasupathy, and A. Rubio, Moiré heterostructures as a condensed-matter quantum simulator, *Nature Physics* **17**, 155 (2021).
- [23] E. Y. Andrei, D. K. Efetov, P. Jarillo-Herrero, A. H. MacDonald, K. F. Mak, T. Senthil, E. Tutuc, A. Yazdani, and A. F. Young, The marvels of moiré materials, *Nature Reviews Materials* **6**, 201 (2021).
- [24] P. Törmä, S. Peotta, and B. A. Bernevig, Superconductivity, superfluidity and quantum geometry in twisted multilayer systems, *Nature Reviews Physics* **4**, 528 (2022).
- [25] D. Guzmán-Silva, C. Mejía-Cortés, M. A. Bandres, M. C. Rechtsman, S. Weimann, S. Nolte, M. Segev, A. Szameit, and R. A. Vicencio, Experimental observation of bulk and edge transport in photonic Lieb lattices, *New Journal of Physics* **16**, 063061 (2014).
- [26] S. Xia, A. Ramachandran, S. Xia, D. Li, X. Liu, L. Tang, Y. Hu, D. Song, J. Xu, D. Leykam, S. Flach, and Z. Chen, Unconventional flatband line states in photonic Lieb lattices, *Physical Review Letters* **121**, 263902 (2018).
- [27] C. Cantillano, S. Mukherjee, L. Morales-Inostroza, B. Real, G. Cáceres-Aravena, C. Hermann-Avigliano, R. R. Thomson, and R. A. Vicencio, Observation of localized ground and excited orbitals in graphene photonic ribbons, *New Journal of Physics* **20**, 033028 (2018).
- [28] L. Song, S. Gao, J. Ma, L. Tang, D. Song, Y. Li, and Z. Chen, Multiple flatbands and localized states in photonic super-kagome lattices, *Optics Letters* **48**, 5947 (2023).
- [29] S. Mukherjee, A. Spracklen, D. Choudhury, N. Goldman, P. Öhberg, E. Andersson, and R. R. Thomson, Observation of a localized flat-band state in a photonic Lieb lattice, *Physical review letters* **114**, 245504 (2015).
- [30] J. Yang, Y. Li, Y. Yang, X. Xie, Z. Zhang, J. Yuan, H. Cai, D.-W. Wang, and F. Gao, Realization of all-band-flat photonic lattices, *Nature Communications* **15**, 1484 (2024).
- [31] S. Kajiwara, Y. Urade, Y. Nakata, T. Nakanishi, and M. Kitano, Observation of a nonradiative flat band for spoof surface plasmons in a metallic Lieb lattice, *Physical Review B* **93**, 075126 (2016).
- [32] Y. Nakata, T. Okada, T. Nakanishi, and M. Kitano, Observation of flat band for terahertz spoof plasmons in a metallic kagomé lattice, *Physical Review B* **85**, 205128 (2012).
- [33] T. Jacqmin, I. Carusotto, I. Sagnes, M. Abbarchi, D. Solnyshkov, G. Malpuech, E. Galopin, A. Lemaître, J. Bloch, and A. Amo, Direct observation of Dirac cones and a flatband in a honeycomb lattice for polaritons, *Physical review letters* **112**, 116402 (2014).
- [34] F. Baboux, L. Ge, T. Jacqmin, M. Biondi, E. Galopin, A. Lemaître, L. Le Gratiet, I. Sagnes, S. Schmidt, H. E. Türeci, A. Amo, and J. Bloch, Bosonic condensation and disorder-induced localization in a flat band, *Physical review letters* **116**, 066402 (2016).
- [35] T. H. Harder, O. A. Egorov, C. Krause, J. Beierlein, P. Gagel, M. Emmerling, C. Schneider, U. Peschel, S. Höfling, and S. Klemmt, Kagome flatbands for coherent exciton-polariton lasing, *ACS Photonics* **8**, 3193 (2021).
- [36] S. Yan, H. Li, J. Yang, X. Chen, H. Liu, D. Dai, R. Zhu, Z. Ma, S. Shi, L. Yang, Y. Yuan, W. Dai, D. Dai, B. Fu, Z. Zuo, H. Ni, Z. Niu, C. Wang, K. Jin, Q. Gong, and X. Xu, Cavity quantum electrodynamics with moiré photonic crystal nanocavity, *Nature Communications* **16**, 4634 (2025).
- [37] P. Wang, Y. Zheng, X. Chen, C. Huang, Y. V. Kartashov, L. Torner, V. V. Konotop, and F. Ye, Localization and delocalization of light in photonic moiré lattices, *Nature* **577**, 42 (2020).
- [38] Q. Jing, Z. Che, S. Chen, T. Xue, J. Wang, W. Liu, Y. Dai, L. Shi, and J. Zi, Observation of Bloch flatbands and localized states in moiré bilayer grating, *Nano Letters* **25**, 12118 (2025).
- [39] C.-H. Yi, H. C. Park, and M. J. Park, Strong interlayer coupling and stable topological flat bands in twisted bilayer photonic moiré superlattices, *Light: Science & Applications* **11**, 289 (2022).
- [40] X.-R. Mao, Z.-K. Shao, H.-Y. Luan, S.-L. Wang, and R.-M. Ma, Magic-angle lasers in nanostructured moiré superlattice, *Nature Nanotechnology* **16**, 1099 (2021).
- [41] H.-Y. Luan, Y.-H. Ouyang, Z.-W. Zhao, W.-Z. Mao, and R.-M. Ma, Reconfigurable moiré nanolaser arrays with phase synchronization, *Nature* **624**, 282 (2023).
- [42] R. Barczyk, L. Kuipers, and E. Verhagen, Observation of Landau levels and chiral edge states in photonic crystals through pseudomagnetic fields induced by synthetic strain, *Nature Photonics* **18**, 574 (2024).
- [43] H. Qin, W. Zhang, S. Chen, H. Zhang, R. Pan, J. Li, L. Shi, J. Zi, and X. Zhang, Quasi-bound flat bands in the continuum, *Nature Communications* **16**, 10835 (2025).
- [44] H.-R. Xia, Z. Wang, Y. Wang, Z. Gao, and M. Xiao, Observation of fully flat bands in a photonic dipolar kagome lattice (2025), arXiv:2509.12843 [physics.optics].
- [45] R. Amedalor, P. Karvinen, H. Pesonen, J. Turunen, T. Niemi, and S. Bej, High-Q guided-mode resonance of a crossed grating with near-flat dispersion, *Applied Physics Letters* **122** (2023).
- [46] H. S. Nguyen, F. Dubois, T. Deschamps, S. Cuffe, A. Pardon, J.-L. Leclercq, C. Seassal, X. Letartre, and P. Viktorovitch, Symmetry breaking in photonic crystals: on-demand dispersion from flatband to Dirac cones, *Physical review letters* **120**, 066102 (2018).
- [47] N. D. Le, P. Bouteyre, A. Kheir-Aldine, F. Dubois, S. Cuffe, L. Berguiga, X. Letartre, P. Viktorovitch, T. Benyattou, and H. S. Nguyen, Super bound states in the continuum on a photonic flatband: Concept, experimental realization, and optical trapping demonstration, *Physical Review Letters* **132**, 173802 (2024).
- [48] M. Choi, A. Alù, and A. Majumdar, Observation of photonic chiral flatbands, *Physical Review Letters* **134**, 103801 (2025).
- [49] S. Eyvazi, E. A. Mamonov, R. Heilmann, J. Cuerda, and P. Törmä, Flat-band lasing in silicon waveguide-

- integrated metasurfaces, *ACS Photonics* **12**, 1570 (2025).
- [50] T. T. H. Do, Z. Yuan, E. G. Durmusoglu, H. K. Shamkhi, V. Valuckas, C. Zhao, A. I. Kuznetsov, H. V. Demir, C. Dang, H. S. Nguyen, and S. T. Ha, Room-temperature lasing at flatband bound states in the continuum, *ACS Nano* **19**, 19287 (2025).
- [51] M. Choi, C. Munley, A. Manna, J. Fröch, A. Barnard, and A. Majumdar, All-dielectric metasurface with a two-dimensional locally flat photonic band (2025), arXiv:2506.20871 [physics.optics].
- [52] K. Sun, Y. Cai, Y. Kivshar, and Z. Han, Flatband high-Q metasurfaces inspired by coupled-resonator optical waveguides, *Advanced Photonics* **7**, 10.1117/1.AP.7.5.056008 (2025).
- [53] S. Zou and G. C. Schatz, Silver nanoparticle array structures that produce giant enhancements in electromagnetic fields, *Chemical Physics Letters* **403**, 62 (2005).
- [54] B. Augu e and W. L. Barnes, Collective resonances in gold nanoparticle arrays, *Physical Review Letters* **101**, 143902 (2008).
- [55] V. G. Kravets, F. Schedin, and A. N. Grigorenko, Extremely narrow plasmon resonances based on diffraction coupling of localized plasmons in arrays of metallic nanoparticles, *Physical Review Letters* **101**, 087403 (2008).
- [56] W. Wang, M. Ramezani, A. I. V akev ainen, P. T orm a, J. G. Rivas, and T. W. Odom, The rich photonic world of plasmonic nanoparticle arrays, *Materials Today* **21**, 303 (2018).
- [57] R. Guo, T. K. Hakala, and P. T orm a, Geometry dependence of surface lattice resonances in plasmonic nanoparticle arrays, *Physical Review B* **95**, 155423 (2017).
- [58] T. Egami and S. Billinge, *Underneath the Bragg Peaks*, 1st ed., edited by R. W. Cahn, Vol. 6 (Elsevier, 2003) pp. 27–31.
- [59] R. J. Moerland, T. K. Hakala, J.-P. Martikainen, H. T. Rekola, A. I. V akev ainen, and P. T orm a, Strong coupling between organic molecules and plasmonic nanostructures, in *Quantum Plasmonics*, Vol. 185, edited by S. I. Bozhevolnyi, L. Martin-Moreno, and F. Garcia-Vidal (Springer International Publishing, 2017) pp. 121–150.
- [60] V. G. Kravets, A. V. Kabashin, W. L. Barnes, and A. N. Grigorenko, Plasmonic surface lattice resonances: A review of properties and applications, *Chemical Reviews* **118**, 5912 (2018).
- [61] H. T. Rekola, T. K. Hakala, and P. T orm a, One-dimensional plasmonic nanoparticle chain lasers, *ACS Photonics* **5**, 1822 (2018).
- [62] D. Wang, A. Yang, A. J. Hryn, G. C. Schatz, and T. W. Odom, Superlattice plasmons in hierarchical Au nanoparticle arrays, *ACS Photonics* **2**, 1789 (2015).
- [63] D. Wang, A. Yang, W. Wang, Y. Hua, R. D. Schaller, G. C. Schatz, and T. W. Odom, Band-edge engineering for controlled multi-modal nanolasing in plasmonic superlattices, *Nature Nanotechnology* **12**, 889 (2017).
- [64] D. Wang, J. Hu, G. C. Schatz, and T. W. Odom, Superlattice surface lattice resonances in plasmonic nanoparticle arrays with patterned dielectrics, *The Journal of Physical Chemistry Letters* **14**, 8525 (2023).
- [65] G. Vecchi, V. Giannini, and J. G. Rivas, Shaping the fluorescent emission by lattice resonances in plasmonic crystals of nanoantennas, *Physical Review Letters* **102**, 146807 (2009).
- [66] M. Auer-Berger, V. Tretnak, F.-P. Wenzl, and J. R. Krenn, Adjusting the emission color of organic light-emitting diodes through aluminum nanodisc arrays, *Optical Engineering* **56**, 1 (2017).
- [67] M. Auer-Berger, V. Tretnak, F.-P. Wenzl, J. R. Krenn, and E. J. W. List-Kratochvil, Aluminum-nanodisc-induced collective lattice resonances: Controlling the light extraction in organic light emitting diodes, *Applied Physics Letters* **111**, 173301 (2017).
- [68] M. Auer-Berger, V. Tretnak, C. Sommer, F.-P. Wenzl, J. R. Krenn, and E. J. W. List-Kratochvil, Multipitched plasmonic nanoparticle grating for broadband light enhancement in white light-emitting organic diodes, *Applied Physics A* **128**, 751 (2022).
- [69] M. S. Abdelkhalik, A. Vaskin, T. L opez, A. M. Berghuis, A. Abass, and J. G. Rivas, Surface lattice resonances for beaming and outcoupling green μ LEDs emission, *Nanophotonics* **12**, 3553 (2023).
- [70] G. Lozano, D. J. Louwers, S. R. Rodr iguez, S. Murai, O. T. Jansen, M. A. Verschuuren, and J. G. Rivas, Plasmonics for solid-state lighting: enhanced excitation and directional emission of highly efficient light sources, *Light: Science & Applications* **2**, e66 (2013).
- [71] R. Heilmann, J. Lehtikoinen, S. Eyvazi, E. A. Mamonov, and P. T orm a, Chains of nanoparticles for flat band emission and lasing (2026), submitted; companion manuscript.
- [72] J. Lehtikoinen, R. Heilmann, A. J. J. Dahlberg, E. H arm a, M. Mahmoudi, A. Dutta, K. S. Daskalakis, and P. T orm a, Data for: Flat bands from diffraction in periodic systems, 10.5281/zenodo.18314492 (2026).